Phonon-limited mobility in n-type single-layer MoS2 from first principles

Kaasbjerg, Kristen; Thygesen, Kristian S.; Jacobsen, Karsten W.

Published in:
Physical Review B Condensed Matter

Link to article, DOI:
10.1103/PhysRevB.85.115317

Publication date:
2012

Document Version
Publisher's PDF, also known as Version of record

Phonon-limited mobility in *n*-type single-layer MoS_2 from first principles

Kristen Kaasbjerg,* Kristian S. Thygesen, and Karsten W. Jacobsen
Center for Atomic-scale Materials Design (CAMD), Department of Physics, Technical University of Denmark, DK-2800 Kgs. Lyngby, Denmark

(Received 14 October 2011; published 23 March 2012)

We study the phonon-limited mobility in intrinsic *n*-type single-layer MoS_2 for temperatures $T > 100$ K. The materials properties including the electron-phonon interaction are calculated from first principles and the deformation potentials and Fröhlich interaction in single-layer MoS_2 are established. The calculated room-temperature mobility of $\sim$410 $cm^2V^{-1}s^{-1}$ is found to be dominated by optical phonon scattering via intra and intervalley deformation potential couplings and the Fröhlich interaction. The mobility is weakly dependent on the carrier density and follows a $\mu \sim T^{-\gamma}$ temperature dependence with $\gamma = 1.69$ at room temperature. It is shown that a quenching of the characteristic homopolar mode, which is likely to occur in top-gated samples, increases the mobility with $\sim$70 $cm^2V^{-1}s^{-1}$ and can be observed as a decrease in the exponent to $\gamma = 1.52$. In comparison to recent experimental findings for the mobility in single-layer MoS_2 ($\sim$200 $cm^2V^{-1}s^{-1}$), our results indicate that mobilities close to the intrinsic phonon-limited mobility can be achieved in two-dimensional materials via dielectric engineering that effectively screens static Coulomb scattering on, e.g., charged impurities.

DOI: 10.1103/PhysRevB.85.115317 PACS number(s): 81.05.Hd, 72.10.−d, 72.20.−i, 72.80.Jc

I. INTRODUCTION

Alongside with the rise of graphene and the exploration of its unique electronic properties,[1–3] the search for other two-dimensional (2D) materials with promising electronic properties has gained increased interest.[4] Metal dichalcogenides, which are layered materials similar to graphite, provide interesting candidates. Their layered structure with weak interlayer van der Waals bonds allows for fabrication of single- to few-layer samples using mechanical peeling/cleavage or chemical exfoliation techniques similar to the fabrication of graphene.[5–8] However, in contrast to graphene, they are semiconductors and hence come with a naturally occurring band gap—a property essential for electronic applications.

The electronic, optical, and vibrational properties of single- to few-layer MoS_2 samples have recently been studied extensively using various experimental techniques.[5,6,8–13] In contrast to the bulk material that has an indirect gap, it has been demonstrated that single-layer MoS_2 is a direct-gap semiconductor with a gap of 1.8 eV.[10,13] Together with the excellent electrostatic control inherent of two-dimensional materials, the large band gap makes it well suited for low-power applications.[14] So far, electrical characterizations of single-layer MoS_2 have shown *n*-type conductivity with room-temperature mobilities in the range 0.5−3 $cm^2V^{-1}s^{-1}$.[5,6,8] Compared to early studies of the intralayer mobility of bulk MoS_2 where mobilities in the range 100−260 $cm^2V^{-1}s^{-1}$ were reported,[15] this is rather low. In a recent experiment, the use of a high-κ gate dielectric in a top-gated device was shown to boost the carrier mobility to a value of $\sim$200 $cm^2V^{-1}s^{-1}$.[8] The observed increase in the mobility was attributed to screening of impurities by the high-κ dielectric and/or modifications of MoS_2 phonons in the top-gated sample.

In order to shed further light on the measured mobilities and the possible role of phonon damping due to a top-gate dielectric,[8] we have carried out a detailed study of the phonon-limited mobility in single-layer MoS_2. Since phonon scattering is an intrinsic scattering mechanism that often dominates at room temperature, the theoretically predicted phonon-limited mobility sets an upper limit for the experimentally achievable mobilities in single-layer MoS_2.[16] In experimental situations, the temperature dependence of the mobility can be useful for the identification of dominating scattering mechanisms and helps to establish the value of the intrinsic electron-phonon couplings.[17] However, the existence of additional extrinsic scattering mechanisms often complicates the interpretation. For example, in graphene samples, impurity scattering and scattering on surface polar optical phonons of the gate oxide are important mobility-limiting factors.[18–23] It can therefore be difficult to establish the value and nature of the intrinsic electron-phonon interaction from experiments alone. Theoretical studies therefore provide useful information for the interpretation of experimentally measured mobilities.

In the present work, the electron-phonon interaction in single-layer MoS_2 is calculated from first principles using a density-functional-based approach. From the calculated electron-phonon couplings, the acoustic and optical deformation potentials (ADP and ODP, respectively) and the Fröhlich interaction in single-layer MoS_2 are inferred. Using these as inputs in the Boltzmann equation, the phonon-limited mobility is calculated in the high-temperature regime ($T >$

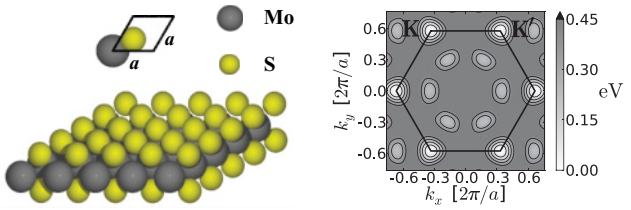

FIG. 1. (Color online) Atomic structure and conduction band of single-layer MoS_2. (Left) Primitive unit cell and structure of an MoS_2 layer with the molybdenum and sulfur atoms positioned in displaced hexagonal layers. (Right) Contour plot showing the lowest-lying conduction band valleys as obtained with DFT-LDA in the hexagonal Brillouin zone of single-layer MoS_2. For *n*-type MoS_2, the low-field mobility is determined by the carrier properties in the K, K' valleys, which are separated in energy from the satellite valleys inside the Brillouin zone.

100 K) where phonon scattering often dominates the mobility. Our findings demonstrate that the calculated phonon-limited room-temperature mobility of $\sim 410\ \mathrm{cm^2 V^{-1} s^{-1}}$ is dominated by optical deformation potential and polar optical scattering via the Fröhlich interaction. The dominating deformation potentials of $D^0_{\mathrm{HP}} = 4.1 \times 10^8$ eV/cm and $D^0_{\mathrm{LO}} = 2.6 \times 10^8$ eV/cm originate from the couplings to the homopolar (HP) and the intervalley polar LO phonons. This is, in contrast to previous studies for bulk MoS_2, where the mobility has been assumed to be dominated entirely by scattering on the homopolar mode.[15,24,25] Furthermore, we show that a quenching of the characteristic homopolar mode, which is polarized in the direction normal to the MoS_2 layer, can be observed as a change in the exponent γ of the generic temperature dependence $\mu \sim T^{-\gamma}$ of the mobility. Such a quenching can be expected to occur in top-gated samples where the MoS_2 layer is sandwiched between a substrate and a gate oxide.

The paper is organized as follows. In Sec. II, the band structure and phonon dispersion of single-layer MoS_2 as obtained with DFT-LDA are presented. The latter is required for the calculation of the electron-phonon coupling presented in Sec. III. From the calculated electron-phonon couplings, we extract zero- and first-order deformation potentials for both intra and intervalley phonons. In addition, the coupling constant for the Fröhlich interaction with the polar LO phonon is determined. In Sec. IV, the calculation of the phonon-limited mobility within the Boltzmann equation is outlined. This includes a detailed treatment of the phonon collision integral from which the scattering rates for the different coupling mechanisms can be extracted. In Sec. V, we present the calculated mobilities as a function of carrier density and temperature. Finally, in Sec. VI, we summarize and discuss our findings.

II. ELECTRONIC STRUCTURE AND PHONON DISPERSION

The electronic structure and phonon dispersion of single-layer MoS_2 have been calculated within DFT in the LDA approximation using a real-space projector-augmented wave (PAW) method.[26–28] The equilibrium lattice constant of the hexagonal unit cell shown in Fig. 1 was found to be $a = 3.14$ Å using a 11×11 **k**-point sampling of the Brillouin zone. In order to eliminate interactions between the layers due to periodic boundary conditions, a large interlayer distance of 10 Å has been used in the calculations.

A. Band structure

In the present study, the band structure of single-layer MoS_2 is calculated within DFT-LDA.[29,30] While DFT-LDA, in general, underestimates band gaps, the resulting dispersion of individual bands, i.e., effective masses and energy differences between valleys, is less problematic. We note, however, that recent GW quasiparticle calculations, which, in general, give a better description of the band structure in standard semiconductors,[54] suggest that the conduction-band minimum is not located at the K, K' points as suggested by DFT-LDA, but rather occur along the path between the Γ and K points in the BZ (the T point).[55,56] This, however, seems to contradict with the experimental consensus that single-layer MoS_2 is a direct-gap semiconductor[10,13] and further studies are needed to clarify this issue. In the following, we therefore use the DFT-LDA band structure and comment on the possible consequences of a valley inversion in Sec. VI.

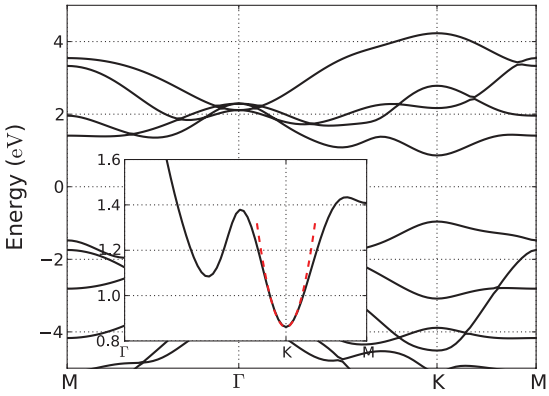

FIG. 2. (Color online) Band structure of single-layer MoS_2. The inset shows a zoom of the conduction band along the path Γ-K-M. The parabolic band (red dashed line) with effective mass $m^* = 0.48\ m_e$ is seen to give a perfect description of the conduction band valley in the K point for the range of energies relevant for the low-field mobility.

The calculated DFT-LDA band structure is shown in Fig. 2. It predicts a direct band gap of 1.8 eV at the K point in the Brillouin zone. The inset shows a zoom of the bottom of the conduction band along the Γ-K-M path in the Brillouin zone. As demonstrated by the dashed line, the conduction band is perfectly parabolic in the K valley. Furthermore, the satellite valley positioned on the path between the Γ and the K points lies on the order of ∼200 meV above the conduction band edge and is therefore not relevant for the low-field transport.

The right plot in Fig. 1 shows a contour plot of the lowest lying conduction band valleys in the two-dimensional Brillouin zone. Here, the K, K' valleys that are populated in n-type MoS_2, are positioned at the corners of the hexagonal Brillouin zone. Due to their isotropic and parabolic nature, the part of the conduction band relevant for the low-field mobility can to a good approximation be described by simple parabolic bands:

$$\varepsilon_{\mathbf{k}} = \frac{\hbar^2 k^2}{2m^*} \tag{1}$$

with an effective electron mass of $m^* = 0.48\ m_e$ and where k is measured with respect to the K, K' points in the Brillouin zone. The two-dimensional nature of the carriers results in a constant density of states given by $\rho_0 = g_s g_v m^*/2\pi\hbar^2$, where $g_s = 2$ and $g_v = 2$ are the spin and K, K'-valley degeneracy, respectively. The large density of states, which follows from the high effective mass of the conduction band in the K, K' valleys, results in nondegenerate carrier distributions except for very high carrier densities.

B. Phonon dispersion

The phonon dispersion has been obtained with the supercell-based small-displacement method[31] using a 9×9 supercell. The resulting phonon dispersion shown in Fig. 3 is

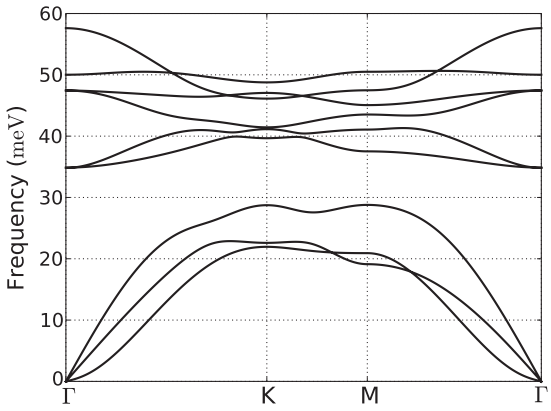

FIG. 3. Phonon dispersion of single-layer MoS_2 calculated with the small displacement method (see, e.g., Ref. 31) using a 9×9 supercell. The frequencies of the two optical Raman active E_{2g} and A_{1g} modes at 48 and 50 meV, respectively, are in excellent agreement with recent experimental measurements (see Ref. 9).

in excellent agreement with recent calculations of the lattice dynamics in two-dimensional MoS_2.[32,33]

With three atoms in the unit cell, single-layer MoS_2 has nine phonon branches—three acoustic and six optical branches. Of the three acoustic branches, the frequency of the out-of-plane flexural mode is quadratic in q for $q \to 0$. In the long-wavelength limit, the frequency of the remaining transverse acoustic (TA) and longitudinal acoustic (LA) modes are given by the in-plane sound velocity c_λ as

$$\omega_{\mathbf{q}\lambda} = c_\lambda q. \tag{2}$$

Here, the sound velocity is found to be 4.4×10^3 and 6.5×10^3 m/s for the TA and LA modes, respectively.

The gap in the phonon dispersion completely separates the acoustic and optical branches even at the high-symmetry points at the zone-boundary where the acoustic and optical modes become similar. The two lowest optical branches belong to the nonpolar optical modes. Due to an insignificant coupling to the charge carriers, they are not relevant for the present study.

The next two branches with a phonon energy of ∼48 meV at the Γ point are the transverse (TO) and longitudinal (LO) polar optical modes where the Mo and S atoms vibrate in counterphase. In bulk polar materials, the coupling of the lattice to the macroscopic polarization setup by the lattice vibration of the polar LO mode results in the so-called LO-TO splitting between the two modes in the long-wavelength limit. The inclusion of this effect from first principles requires knowledge of the Born effective charges.[34–36] In two-dimensional materials, however, the lack of periodicity in the direction perpendicular to the layer removes the LO-TO splitting.[37] The coupling to the macroscopic polarization of the LO mode will therefore be neglected here.

The almost dispersionless phonon at ∼50 meV is the so-called homopolar mode, which is characteristic for layered structures. The lattice vibration of this mode corresponds to a change in the layer thickness and has the sulfur layers vibrating in counterphase in the direction normal to the layer plane, while the Mo layer remains stationary. The change in the potential associated with this lattice vibration has previously been demonstrated to result in a large deformation potential in bulk MoS_2.[15]

III. ELECTRON-PHONON COUPLING

In this section, we present the electron-phonon coupling in single-layer MoS_2 obtained with a first-principles-based DFT approach. The method is based on a supercell approach analogous to that used for the calculation of the phonon dispersion and is outlined in Appendix A. The calculated electron-phonon couplings are discussed in the context of deformation potential couplings and the Fröhlich interaction well known from the semiconductor literature.

Within the adiabatic approximation for the electron-phonon interaction, the coupling strength for the phonon mode with wave vector $\mathbf{q}$ and branch index λ is given by

$$g^\lambda_{\mathbf{kq}} = \sqrt{\frac{\hbar}{2MN\omega_{\mathbf{q}\lambda}}} M^\lambda_{\mathbf{kq}}, \tag{3}$$

where $\omega_{\mathbf{q}\lambda}$ is the phonon frequency, M is an appropriately defined effective mass, N is the number of unit cells in the crystal, and

$$M^\lambda_{\mathbf{kq}} = \langle \mathbf{k}+\mathbf{q}|\delta V_{\mathbf{q}\lambda}(\mathbf{r})|\mathbf{k}\rangle \tag{4}$$

is the coupling matrix element, where $\mathbf{k}$ is the wave vector of the carrier being scattered and $\delta V_{\mathbf{q}\lambda}$ is the change in the effective potential per unit displacement along the vibrational normal mode.

Due to the valley degeneracy in the conduction band, both intra and intervalley phonon scattering of the carriers in the K, K' valleys need to be considered. Here, the coupling constants for these scattering processes are approximated by the electron-phonon coupling at the bottom of the valleys, i.e., with $\mathbf{k} = \mathbf{K}, \mathbf{K}'$. With this approach, the intra and intervalley scattering for the K, K' valleys are thus assumed independent on the wave vector of the carriers.

In the following two sections, the calculated electron-phonon couplings are presented.[38] The different deformation potential couplings are discussed and the functional form of the Fröhlich interaction in 2D materials is established. Piezoelectric coupling to the acoustic phonons that is present in materials without inversion symmetry, is most important at low temperatures[39] and will not be considered here. Since deformation potentials are often extracted as empirical parameters from experimental mobilities, it can be difficult to disentangle contributions from different phonons. Here, the first-principles calculation of the electron-phonon coupling allows a detailed analysis of the couplings and the assignments of deformation potentials to the individual intra and intervalley phonons.

A. Deformation potentials

The deformation potential interaction describes how carriers interact with the local changes in the crystal potential associated with a lattice vibration. Within the deformation potential approximation, the electron-phonon coupling is

expressed as[40]

$$g_{\mathbf{q}\lambda} = \sqrt{\frac{\hbar}{2A\rho\omega_{\mathbf{q}\lambda}}} M_{\mathbf{q}\lambda}, \tag{5}$$

where A is the area of the sample, ρ is the atomic mass density per area, and $M_{\mathbf{q}\lambda}$ is the coupling matrix element for a given valley which is assumed independent on the $\mathbf{k}$ vector of the carriers. This expression follows from the general definition of the electron-phonon coupling in Eq. (3) by setting the effective mass M equal to the sum of the atomic masses in the unit cell. With this convention for the effective mass, $MN = A\rho$, and the expression in Eq. (5) is obtained.

For scattering on acoustic phonons, the coupling matrix element is linear in q in the long-wavelength limit,

$$M_{\mathbf{q}\lambda} = \Xi_\lambda q, \tag{6}$$

where Ξ_λ is the acoustic deformation potential.

In the case of optical phonon scattering, both coupling to zero and first order in q must be considered. The interaction via the constant zero-order optical deformation potential D^0_λ is given by

$$M_{\mathbf{q}\lambda} = D^0_\lambda. \tag{7}$$

The coupling via the zero-order deformation potential is dictated by selection rules for the coupling matrix elements. Therefore only symmetry-allowed phonons can couple to the carriers via the zero-order interaction. The coupling via the first-order interaction is given by Eq. (6) with the acoustic deformation potential replaced by the first-order optical deformation potential D^1_λ. Both the zero- and first-order deformation potential coupling can give rise to intra and intervalley scattering.

The absolute value of the calculated coupling matrix elements $|M_{\mathbf{q}\lambda}|$ are shown in Fig. 4 for the phonons that couple to the carriers via deformation potential interactions. They are plotted in the range of phonon wave vectors relevant for intra and intervalley scattering processes,[41] and only phonon modes with significant coupling strengths have been included. Although the coupling matrix elements are shown only for $\mathbf{k} = \mathbf{K}$, the matrix elements for $\mathbf{k} = \mathbf{K}'$ are related through time-reversal symmetry as $M^{\mathbf{K}}_{\mathbf{q}\lambda} = M^{\mathbf{K}'}_{-\mathbf{q}\lambda}$ leading to different directions of anisotropy in the K, K' valleys. The three-fold rotational symmetry of the coupling matrix elements in $\mathbf{q}$-space stems from the symmetry of the conduction band in the vicinity of the K, K' valleys (see Fig. 1). Since the symmetry of the matrix elements has not been imposed by hand, slight deviations from the three-fold rotational symmetry can be observed.

The acoustic deformation potential couplings for the TA and LA modes are shown in the two top plots of Fig. 4. Due to the inclusion of umklapp processes here, the coupling to the TA mode does not vanish as is most often assumed.[42] Only along high-symmetry directions in the Brillouin zone, this is the case. This results in a highly anisotropic coupling to the TA mode. On the other hand, the deformation potential coupling for the LA mode is perfectly isotropic in the long-wavelength limit but also becomes anisotropic at shorter wavelengths. In agreement with Eq. (6), both the TA and LA coupling matrix elements are linear in q in the long-wavelength limit.

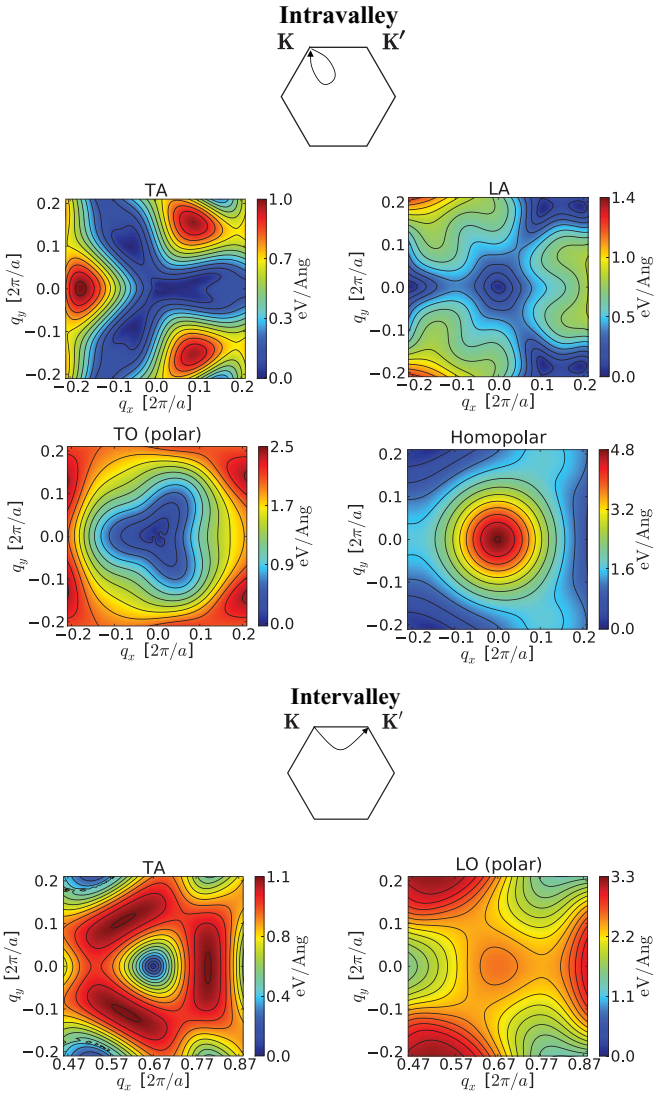

FIG. 4. (Color online) Deformation potential couplings in single-layer MoS_2. Only phonon modes with significant coupling strength are shown. The contour plots show the absolute value of the coupling matrix elements $|M_{\mathbf{q}\lambda}|$ in Eq. (4) with $\mathbf{k} = \mathbf{K}$ and $\mathbf{k}' = \mathbf{K} + \mathbf{q}$ as a function of the two-dimensional phonon wave vector $\mathbf{q}$ (note the different color scales in the plots). The upper four plots correspond to intravalley scattering and the two bottom plots to intervalley scattering on phonons with wave vector $\mathbf{q} = 2\mathbf{K}$. The two zero-order deformation potential couplings to the intravalley homopolar and intervalley LO phonon play an important role for the room-temperature mobility.

The next two plots show the couplings to the intravalley polar TO and homopolar optical modes. While the interaction with the polar TO phonon corresponds to a first-order optical deformation potential, the interaction with the homopolar mode acquires a finite value of ~4.8 eV/Å in the Γ point and corresponds to a strong zero-order deformation potential coupling. The large deformation potential coupling to the homopolar mode stems from its characteristic lattice vibration polarized in the direction perpendicular to the layer corresponding to a change in the layer thickness. The associated change in the crystal potential from the counterphase

oscillation of the two negatively charged sulfur layers results in a significant change of the potential toward the center of the MoS_2 layer. As the electronic Bloch functions have significant weight here, the homopolar lattice vibration gives rise to a significant shift of the K, K'-valley states. The large deformation potential associated with the coupling to the homopolar mode is also present in bulk MoS_2.[15]

The two bottom plots in Fig. 4 show the couplings for the intervalley TA and polar LO phonons. Due to the nearly constant frequency of the intervalley acoustic phonons, their couplings are equivalent to optical deformation potential couplings. Both the coupling to the intervalley TA phonon and the coupling to the intervalley LA phonon (not shown in Fig. 4) correspond to first-order deformation potentials. The intervalley coupling for the polar LO phonon gives rise to a zero-order deformation potential that results from an identical in-plane motion of the two sulfur layers in the lattice vibration of the LO intervalley phonon.

In general, the deformation potential approximation, i.e., the assumption of isotropic and constant/linear coupling matrix elements, in Eqs. (6) and (7) is seen to hold in the long-wavelength limit only. At shorter wavelengths, the first-principles couplings become anisotropic and have a more complicated q dependence. When deformation potentials are determined experimentally from, e.g., the temperature dependence of the mobility,[17] they represent *effective* couplings that implicitly account for the more complex $\mathbf{q}$ dependence of the *true* coupling matrix elements and their different directions of anisotropy in degenerate valleys.

In Sec. V, the *effective* deformation potentials for single-layer MoS_2 are determined from the calculated first-principles electron-phonon couplings. This is done by fitting their associated scattering rates to the scattering rates obtained with the first-principles coupling matrix elements. The resulting deformation potentials can be applied directly in practical transport calculations based on, e.g., the Boltzmann equation or Monte Carlo simulations. Similar routes for first-principles calculations of deformation potentials have been given in the literature.[43–45]

B. Fröhlich interaction

The lattice vibration of the polar LO phonon gives rise to a macroscopic electric field that couples to the charge carriers. For bulk three-dimensional systems, the coupling to the electric field is given by the Fröhlich interaction,[42]

$$g_{\mathrm{LO}}(q) = \frac{1}{q}\sqrt{\frac{e^2\hbar\omega_{\mathrm{LO}}}{2\epsilon_0 V}}\left(\frac{1}{\varepsilon^{\infty}} - \frac{1}{\varepsilon^{0}}\right)^{1/2}, \tag{8}$$

which diverges as $1/q$ in the long-wavelength limit and where ϵ_0 is the vacuum permittivity, V is the volume of the sample, and ε^{∞} and ε^{0} are the high-frequency optical and static dielectric constant, respectively.

In atomically thin materials, the two-dimensional nature of both the LO phonon and the charge carriers leads to a qualitatively different q dependence of the Fröhlich interaction. The situation is here similar to 2D semiconductor heterostructures where the Fröhlich interaction has been studied using dielectric continuum models and microscopic approaches.[46,47] In Appendix B, a microscopic approach based on atomic Born effective charges is used to derive the following nondiverging analytic form for the Fröhlich interaction in 2D materials,

$$g_{\mathrm{LO}}(q) = g_{\mathrm{Fr}}\,\mathrm{erfc}(q\sigma/2). \tag{9}$$

Here, the coupling constant g_{Fr} is the equivalent of the square root factors in Eq. (8), σ is the effective width of the electronic Bloch states, and erfc is the complementary error function.

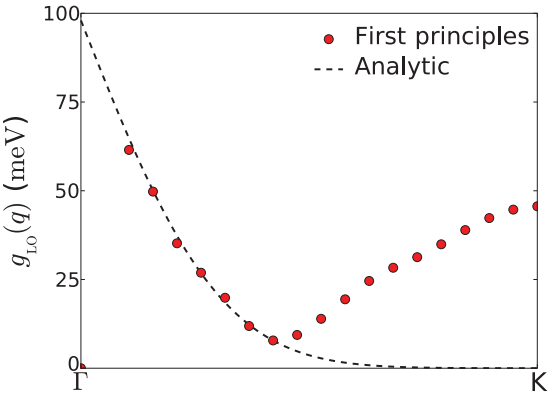

FIG. 5. (Color online) Fröhlich interaction for the polar optical LO mode. The dashed line shows the analytical coupling in Eq. (9) with the coupling constant $g_{\mathrm{Fr}} = 98$ meV and the effective layer thickness $\sigma = 4.41$ Å fitted to the long-wavelength limit of the calculated coupling (dots).

Figure 5 shows the calculated first-principles coupling g_{LO} to the polar LO phonon in single-layer MoS_2 (dots) as a function of the phonon wave vector along the Γ-K path. The dashed line shows a fit of the analytic coupling in Eq. (9) to the long-wavelength limit of the first-principles coupling. A coupling constant $g_{\mathrm{Fr}} = 98$ meV and an effective width $\sigma = 4.41$ Å are found to give a perfect fit to the calculated coupling in the long-wavelength limit. For shorter wavelengths, the zero-order deformation potential coupling to the intervalley LO phonon from Fig. 4 becomes dominant, and a deviation away from the analytic behavior in Eq. (9) is observed.

IV. BOLTZMANN EQUATION

In the regime of diffuse transport dominated by phonon scattering, the mobility can be obtained with semiclassical Boltzmann transport theory. In the absence of spatial gradients, the Boltzmann equation for the out-of-equilibrium distribution function $f_{\mathbf{k}}$ of the charge carriers reads[48]

$$\frac{\partial f_{\mathbf{k}}}{\partial t} + \dot{\mathbf{k}}\cdot\nabla_{\mathbf{k}} f_{\mathbf{k}} = \left.\frac{\partial f_{\mathbf{k}}}{\partial t}\right|_{\mathrm{coll}}, \tag{10}$$

where the time evolution of the crystal momentum is governed by the applied electric field $\mathbf{E}$ through $\hbar\dot{\mathbf{k}} = q\mathbf{E}$ and q is the charge of the carriers. In the case of a time-independent uniform electric field, the steady-state version of the linearized Boltzmann equation takes the form

$$\frac{q}{\hbar}\mathbf{E}\cdot\nabla_{\mathbf{k}} f^0_{\mathbf{k}} = -\frac{q}{k_{\mathrm{B}}T}\mathbf{E}\cdot\mathbf{v}_{\mathbf{k}} f^0_{\mathbf{k}}\left(1 - f^0_{\mathbf{k}}\right) = \left.\frac{\partial f_{\mathbf{k}}}{\partial t}\right|_{\mathrm{coll}}, \tag{11}$$

where $f^0_{\mathbf{k}} = f^0(\varepsilon_{\mathbf{k}})$ is the equilibrium Fermi-Dirac distribution function, $\partial f^0_{\mathbf{k}}/\partial\varepsilon_{\mathbf{k}} = -f^0_{\mathbf{k}}(1-f^0_{\mathbf{k}})/k_{\mathrm{B}}T$, and $\mathbf{v}_{\mathbf{k}} = \nabla_{\mathbf{k}}\varepsilon_{\mathbf{k}}/\hbar$ is the band velocity. In the linear response regime, the out-of-equilibrium distribution function can be written as the equilibrium function plus a small deviation δf away from its equilibrium value,

$$\delta f_{\mathbf{k}} = f_{\mathbf{k}} - f^0_{\mathbf{k}} = f^0_{\mathbf{k}}\big(1-f^0_{\mathbf{k}}\big)\psi_{\mathbf{k}}, \tag{12}$$

where the last equality has defined the deviation function $\psi_{\mathbf{k}}$.[48] Furthermore, following the spirit of the iterative method of Rode,[49] the angular dependence of the deviation function is separated out as

$$\psi_{\mathbf{k}} = \phi_k \cos\theta_{\mathbf{k}}, \tag{13}$$

where $\theta_{\mathbf{k}}$ is the angle between the $\mathbf{k}$ vector and the force exerted on the carriers by the applied field $\mathbf{E}$. In general, $\phi_{\mathbf{k}}$ is a function of the $\mathbf{k}$ vector and not only its magnitude k. However, for isotropic bands as considered here, the angular dependence of the deviation function is entirely accounted for by the cosine factor in Eq. (13).[40]

Considering scattering on phonons, the collision integral describes how accelerated carriers are driven back toward their equilibrium distribution by scattering on acoustic and optical phonons. In the high-temperature regime of interest here, the collision integral can be split up in two contributions. The first, accounting for the quasielastic scattering on acoustic phonons, can be expressed in the form of a relaxation time τ_{el}. The second, describing the inelastic scattering on optical phonons, will, in general, be an integral operator I_{inel}. The collision integral can thus be written

$$\left.\frac{\partial f_{\mathbf{k}}}{\partial t}\right|_{\mathrm{coll}} = -\frac{\delta f_{\mathbf{k}}}{\tau^{\mathrm{el}}_{\mathbf{k}}} + I_{\mathrm{inel}}[\psi_{\mathbf{k}}], \tag{14}$$

where the explicit forms of the relaxation time and the integral operator will be considered in detail below.

With the above form of the collision integral, the Boltzmann equation can be solved by iterating the equation

$$\phi_k = \left[\frac{eE\upsilon_{\mathbf{k}}}{k_{\mathrm{B}}T} + I'_{\mathrm{inel}}[\phi_k]\right]\left(\frac{1}{\tau^{\mathrm{el}}_{\mathbf{k}}}\right)^{-1} \tag{15}$$

for the deviation function ϕ_k. Here, the angular dependence $\cos\theta_{\mathbf{k}}$ and a $f^0_{\mathbf{k}}(1-f^0_{\mathbf{k}})$ factor have been divided out and the new integral operator I'_{inel} is defined by

$$I_{\mathrm{inel}} = f^0_{\mathbf{k}}\big(1-f^0_{\mathbf{k}}\big)\cos\theta_{\mathbf{k}} I'_{\mathrm{inel}}. \tag{16}$$

From the solution of the Boltzmann equation the current and drift mobility of the carriers can be obtained. Taking the electric field to be oriented along the x direction, the current density is given by

$$j_x \equiv \sigma_{xx}E_x = -\frac{4e}{A}\sum_{\mathbf{k}} v_x \delta f_{\mathbf{k}}, \tag{17}$$

where σ_{xx} is the conductivity, A is the area of the sample, and $v_i = \hbar k_i/m^*$ is the band velocity for parabolic bands with $i = x,y,z$. From the definition $\mu_{xx} = \sigma_{xx}/ne$ of the drift mobility, it follows that

$$\mu_{xx} = \frac{e\langle\tilde{\phi}_k\rangle}{m^*}, \tag{18}$$

where the modified deviation function $\tilde{\phi}_k$ having units of time is defined by

$$\tilde{\phi}_k = \frac{m^* k_{\mathrm{B}}T}{eE_x\hbar k}\phi_k, \tag{19}$$

and the energy-weighted average $\langle\cdot\rangle$ is defined by

$$\langle A\rangle = \frac{1}{n}\int d\varepsilon_{\mathbf{k}}\ \rho(\varepsilon_{\mathbf{k}})\varepsilon_{\mathbf{k}}A_{\mathbf{k}}\left(-\frac{\partial f^0}{\partial\varepsilon_{\mathbf{k}}}\right). \tag{20}$$

Here, n is the two-dimensional carrier density. In the relaxation time approximation, $\tilde{\phi}_k = \tau_k$ and the well-known Drude expression for the mobility $\mu = e\langle\tau_k\rangle/m^*$ is recovered.

A. Phonon collision integral

The phonon collision integral has been considered in great detail in the literature for two-dimensional electron gases in semiconductor heterostructure (see, e.g., Ref. 39). In general, these treatments consider scattering on three-dimensional or quasi two-dimensional phonons. In atomically thin materials, the phonons are strictly two dimensional, which results in a slightly different treatment. In the following, a full account of the two-dimensional phonon collision integral is given for scattering on acoustic and optical phonons.

With the distribution function written on the form in Eq. (12), the linearized collision integral for electron-phonon scattering takes the form[48]

$$\begin{aligned}\left.\frac{\partial f_{\mathbf{k}}}{\partial t}\right|_{\mathrm{coll}} = -\frac{2\pi}{\hbar}\sum_{\mathbf{q}\lambda}\frac{|g_{\mathbf{q}\lambda}|^2}{\epsilon^2(q,T)}\times\Big[&f^0_{\mathbf{k}}\big(1-f^0_{\mathbf{k}+\mathbf{q}}\big)N^0_{\mathbf{q}\lambda}(\psi_{\mathbf{k}}-\psi_{\mathbf{k}+\mathbf{q}})\delta(\varepsilon_{\mathbf{k}+\mathbf{q}}-\varepsilon_{\mathbf{k}}-\hbar\omega_{\mathbf{q}\lambda})\\ &+ f^0_{\mathbf{k}}\big(1-f^0_{\mathbf{k}-\mathbf{q}}\big)\big(1+N^0_{\mathbf{q}\lambda}\big)(\psi_{\mathbf{k}}-\psi_{\mathbf{k}-\mathbf{q}})\delta(\varepsilon_{\mathbf{k}-\mathbf{q}}-\varepsilon_{\mathbf{k}}+\hbar\omega_{\mathbf{q}\lambda})\Big],\end{aligned} \tag{21}$$

where $N^0_{\mathbf{q}\lambda} = N^0(\hbar\omega_{\mathbf{q}\lambda})$ is the equilibrium distribution of the phonons given by the Bose-Einstein distribution function and $f^0_{\mathbf{k}\pm\mathbf{q}} = f^0(\varepsilon_{\mathbf{k}}\pm\hbar\omega_{\mathbf{q}})$ is understood. The different terms inside the square brackets account for scattering out of $(\psi_{\mathbf{k}})$ and into $(\psi_{\mathbf{k}\pm\mathbf{q}})$ the state with wave vector $\mathbf{k}$ via absorption and emission of phonons. Screening of the electron-phonon interaction by the carriers themselves is accounted for by the static dielectric function ϵ, which is both wave vector q and temperature T dependent. For nondegenerate carriers, semiclassical screening where the screening length is given by

the inverse of the Debye-Hückel wave vector $k_D = e^2 n/2k_B T$ applies.[50] In the present study, the considered values of carrier densities and temperatures correspond to Debye-Hückel wave vectors on the order of a few fractions of the Brillouin zone size, i.e., $k_D \ll 2\pi/a$. Since scattering on phonons, in general, involves larger wave vectors, screening by the carriers can to a good approximation be neglected here. The calculated mobilities therefore provide a lower limit for the proper screened mobilities.

1. Quasielastic scattering on acoustic phonons

For quasielastic scattering on acoustic phonons at high temperatures, the energy of the acoustic phonon can be neglected in the collision integral in Eq. (21). As a consequence, the collision integral can be recast in the form of the following relaxation time:[39]

$$\frac{1}{\tau_{\mathbf{k}}^{\mathrm{el}}} = \sum_{\mathbf{k}'} (1 - \cos\theta_{\mathbf{k}\mathbf{k}'}) P_{\mathbf{k}\mathbf{k}'}, \tag{22}$$

where the summation variable has been changed to $\mathbf{k}' = \mathbf{k} \pm \mathbf{q}$ and the transition matrix element for quasielastic scattering on acoustic phonons is given by

$$P_{\mathbf{k}\mathbf{k}'} = \frac{2\pi}{\hbar} \sum_{\mathbf{q}} |g_{\mathbf{q}\lambda}|^2 \left[N^0_{\mathbf{q}\lambda} \delta(\varepsilon_{\mathbf{k}'} - \varepsilon_{\mathbf{k}}) + \left(1 + N^0_{\mathbf{q}\lambda}\right) \delta(\varepsilon_{\mathbf{k}'} - \varepsilon_{\mathbf{k}}) \right]. \tag{23}$$

For isotropic scattering, as assumed here in Eq. (6), the square of the electron-phonon coupling can be expressed as

$$|g_{\mathbf{q}\lambda}|^2 = \frac{\Xi_\lambda^2 \hbar q}{2A\rho c_\lambda}, \tag{24}$$

where the acoustic phonon frequency has been expressed in terms of the sound velocity c_λ. Except at very low temperatures $\hbar\omega_{\mathbf{q}} \ll k_B T$ implying that the equipartition approximation $N^0_{\mathbf{q}} \sim k_B T/\hbar\omega_{\mathbf{q}} \gg 1$ for the Bose-Einstein distribution applies. With the resulting $\mathbf{q}$ factors in the transition matrix element in Eq. (23) canceling, the $\cos\theta_{\mathbf{k}\mathbf{k}'}$ term in the $\mathbf{k}'$ sum in Eq. (22) vanishes and the first term yields a factor density of states divided by the spin and valley degeneracies $\rho_0/g_s g_v$. The resulting relaxation time for acoustic phonon scattering is independent on the carrier energy and is given by

$$\frac{1}{\tau_{\mathbf{k}}^{\mathrm{el}}} = \frac{m^* \Xi^2 k_B T}{\hbar^3 \rho c_\lambda^2}. \tag{25}$$

The independence on the carrier energy and the $\tau^{-1} \sim T$ temperature dependence of the inverse acoustic relaxation time are characteristic for two-dimensional systems and layered materials.[15,39]

2. Inelastic scattering on dispersionless optical phonons

For inelastic scattering on optical phonons, the phonon energy can no longer be neglected and the collision integral in Eq. (21) must be considered in full detail. Under the reasonable assumption of dispersionless optical phonons $\omega_{\mathbf{q}\lambda} = \omega_\lambda$, the inelastic collision integral can be treated semianalytically. The overall procedure for the evaluation of the collision integral is given below, while the calculational details have been collected in Appendix C. The resulting expressions for the collision integral apply to both intravalley and intervalley optical and intervalley acoustic phonons.

In the following, the integral operator for inelastic scattering in Eq. (16) is split up in separate out- and in-scattering contributions,

$$I'_{\mathrm{inel}}[\phi_k] = I'^{\mathrm{out}}_{\mathrm{inel}}[\phi_k] + I'^{\mathrm{in}}_{\mathrm{inel}}[\phi_k], \tag{26}$$

which include the terms in Eq. (21) involving $\psi_{\mathbf{k}}$ and $\psi_{\mathbf{k}\pm\mathbf{q}}$, respectively. With the contributions from different phonon branches λ adding up, scattering on a single phonon with branch index λ is considered in the following.

From Eq. (21), the out-scattering part of the collision integral follows directly as

$$I'^{\mathrm{out}}_{\mathrm{inel}}[\phi_k] = -\phi_k \sum_{\mathbf{k}'} P_{\mathbf{k}\mathbf{k}'} \frac{1 - f^0_{\mathbf{k}'}}{1 - f^0_{\mathbf{k}}}, \tag{27}$$

where the transition matrix element for optical phonon scattering is given by

$$P_{\mathbf{k}\mathbf{k}'} = \frac{2\pi}{\hbar} \sum_{\mathbf{q}} |g_{\mathbf{q}\lambda}|^2 \left[N^0_\lambda \delta(\varepsilon_{\mathbf{k}'} - \varepsilon_{\mathbf{k}} - \hbar\omega_\lambda) + \left(1 + N^0_\lambda\right) \delta(\varepsilon_{\mathbf{k}'} - \varepsilon_{\mathbf{k}} + \hbar\omega_\lambda) \right]. \tag{28}$$

For the in-scattering part, the desired $\cos\theta_{\mathbf{k}}$ factor in Eq. (16) can be extracted from $\psi_{\mathbf{k}'}$ using the relation $\cos\theta_{\mathbf{k}'} = \cos\theta_{\mathbf{k}}\cos\theta_{\mathbf{k}\mathbf{k}'} - \sin\theta_{\mathbf{k}}\sin\theta_{\mathbf{k}\mathbf{k}'}$. Since the sine term vanishes from symmetry consideration, the in-scattering part of the inelastic collision integral reduces to

$$I'^{\mathrm{in}}_{\mathrm{inel}}[\phi_k] = \sum_{\mathbf{k}'} \phi_{k'} \cos\theta_{\mathbf{k}\mathbf{k}'} P_{\mathbf{k}\mathbf{k}'} \frac{1 - f^0_{\mathbf{k}'}}{1 - f^0_{\mathbf{k}}}. \tag{29}$$

The evaluation of the $\mathbf{k}'$ sum in Eqs. (27) and (29) is outlined in Appendix C. Here, the assumption of dispersionless optical phonons allows for a semianalytical treatment. For zero- and first-order coupling within the deformation potential approximation, the sum can be carried out analytically. The resulting expressions for the collision integral are given in Eqs. (C14), (C15), (C16), (C17), and (C18). In the case of the Fröhlich interaction, the angular part of the $\mathbf{q}$ integral must be done numerically.

3. Optical deformation potential scattering rates

In spite of the fact that the collision integral for inelastic scattering on optical phonons cannot be recast in the form of a (momentum) relaxation time,[51] a scattering rate related to the inverse carrier lifetime can still be defined from the out-scattering part of the inelastic collision integral alone. The scattering rate so defined is given by

$$\frac{1}{\tau_{\mathbf{k}}^{\mathrm{inel}}} = \sum_{\mathbf{k}'} P_{\mathbf{k}\mathbf{k}'} \frac{1 - f^0_{\mathbf{k}'}}{1 - f^0_{\mathbf{k}}} \tag{30}$$

and is equivalent to the inverse carrier lifetime given by the imaginary part of the electronic self-energy in the Born approximation.[48] Below, the resulting scattering rates for zero-order and first-order deformation potential scattering are given for nondegenerate carriers, i.e., with the Fermi factors in Eq. (30) neglected. They follow straightforwardly from the

expressions for the out-scattering part of the collision integral derived in Appendix C.

For zero-order deformation potential scattering, the scattering rate is independent of the carrier energy and given by

$$\frac{1}{\tau_{\mathbf{k}}^{\text{inel}}} = \frac{m^*\left(D_\lambda^0\right)^2}{2\hbar^2\rho\omega_\lambda}[1 + e^{\hbar\omega_\lambda/k_BT}\Theta(\varepsilon_{\mathbf{k}} - \hbar\omega_\lambda)]N_\lambda^0. \quad (31)$$

Here, $\Theta(x)$ is the Heavyside step function, which assures that only electrons with sufficient energy can emit a phonon. It should be noted that the scattering rate in Eq. (31) for zero-order deformation potential coupling in fact defines a proper momentum relaxation time because the in-scattering part of the collision integral vanishes in this case (see Appendix C).

The scattering rate for coupling via the first-order deformation potential is found to be

$$\frac{1}{\tau_{\mathbf{k}}^{\text{inel}}} = \frac{m^{*2}\left(D_\lambda^1\right)^2}{\hbar^4\rho\omega_\lambda}[(2\varepsilon_{\mathbf{k}} + \hbar\omega_\lambda) + e^{\hbar\omega_\lambda/k_BT} \times \Theta(\varepsilon_{\mathbf{k}} - \hbar\omega_\lambda)(2\varepsilon_{\mathbf{k}} - \hbar\omega_\lambda)]N_\lambda^0. \quad (32)$$

Due to the linear dependence on the carrier energy, zero-order scattering processes dominate first-order processes at low energies. Only under high-field conditions where the carriers are accelerated to high velocities will first-order scattering become significant.

The expressions for the scattering rates in Eqs. (31) and (32) above apply to scattering on dispersionless intervalley acoustic phonons and intra/intervalley optical phonons. Except for a factor of $\sqrt{\varepsilon_{\mathbf{k}} \pm \hbar\omega_\lambda}$ originating from the density of states, the energy dependence of the scattering rates is identical to that of their three-dimensional analogs.[40]

V. RESULTS

In the following, the scattering rate and phonon-limited mobility in single-layer MoS_2 are studied as a function of carrier energy, temperature T, and carrier density n using the material parameters collected in Table I. Here, the reported deformation potentials represent effective coupling parameters for the deformation potential approximation in Eqs. (6) and (7) (see below).

A. Scattering rates

With access to the first-principles electron-phonon couplings, the scattering rate taking into account the anisotropy and full q dependence of the first-principles coupling matrix elements can be evaluated. They are obtained using the expression for the scattering rate in Eq. (30) with the respective transition matrix elements for acoustic and optical phonon scattering given in Eqs. (23) and (28).[52] The resulting scattering rates are shown in Fig. 6 as a function of the carrier energy for nondegenerate carriers at $T = 300$ K. In order to account for the difference between the coupling matrix elements in the K, K' valleys imposed by time-reversal symmetry, the shown scattering rates are valley-averages defined by $\tau = (\tau_K + \tau_{K'})/2$. The different lines in Fig. 6 show the contributions to the total scattering rate

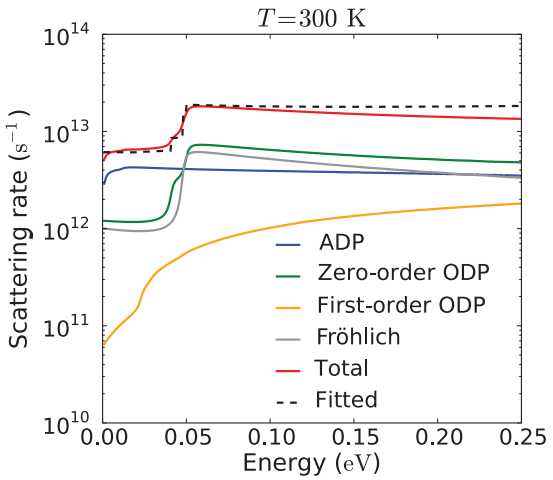

FIG. 6. (Color online) Scattering rates for the different electron-phonon couplings as a function of carrier energy at $T = 300$ K. The scattering rates have been calculated from the first-principles electron-phonon couplings in Figs. 4 and 5. The (black) dashed line shows the scattering rate obtained using the fitted deformation potential parameters defined in Eqs. (6) and (7). The kinks in the curves for the optical scattering rates mark the onset of optical phonon emissions.

from the various electron-phonon couplings to the intra and intervalley phonons that have been grouped according to their coupling type, i.e., acoustic deformation potentials (ADPs), zero/first-order optical deformation potentials (ODPs), and the Fröhlich interaction. The acoustic deformation potential scattering includes the quasielastic intravalley scattering on

TABLE I. Material parameters for single-layer MoS_2. Unless otherwise stated, the parameters have been calculated from first principles as described in the Secs. II and III. The $\mathbf{\Gamma}/\mathbf{K}$ subscript on the optical deformation potentials indicate couplings to the intra/intervalley phonons.

Parameter	Symbol	Value
Lattice constant	a	3.14 Å
Ion mass density	ρ	3.1×10^{-7} g/cm^2
Effective electron mass	m^*	0.48 m_e
Transverse sound velocity	c_{TA}	4.2×10^3 m/s
Longitudinal sound velocity	c_{LA}	6.7×10^3 m/s
Acoustic deformation potentials		
TA	Ξ_{TA}	1.6 eV
LA	Ξ_{LA}	2.8 eV
Optical deformation potentials		
TA	$D^1_{\mathbf{K},\text{TA}}$	5.9 eV
LA	$D^1_{\mathbf{K},\text{LA}}$	3.9 eV
TO	$D^1_{\mathbf{\Gamma},\text{TO}}$	4.0 eV
TO	$D^1_{\mathbf{K},\text{TO}}$	1.9 eV
LO	$D^0_{\mathbf{K},\text{LO}}$	2.6×10^8 eV/cm
Homopolar	$D^0_{\mathbf{\Gamma},\text{HP}}$	4.1×10^8 eV/cm
Fröhlich interaction (LO)		
Effective layer thickness	σ	4.41 Å
Coupling constant	g_{Fr}	98 meV
Optical phonon energies		
Polar LO	$\hbar\omega_{\text{LO}}$	48 meV
Homopolar	$\hbar\omega_{\text{HP}}$	50 meV

the TA and LA phonons with linear dispersions. Scattering on intervalley acoustic phonons is considered as optical deformation potential scattering. Both the total scattering rate and the contributions from the different coupling types have been obtained using Matthiessen's rule by summing the scattering rates from the individual phonons, i.e.,

$$\tau_{\text{tot}}^{-1} = \sum_{\lambda} \tau_{\lambda}^{-1}. \tag{33}$$

For carrier energies below, the optical phonon frequencies, the total scattering rate is dominated by acoustic deformation potential scattering. At higher energies, zero-order deformation potential scattering and polar optical scattering via the Fröhlich interaction become dominant. Due to the linear dependence on the carrier energy, the first-order deformation potential scattering on the intervalley acoustic phonons and the optical phonons is, in general, only of minor importance for the low-field mobility. This is also the case here, where it is an order of magnitude smaller than the other scattering rates for almost the entire plotted energy range. The jumps in the curves for the optical scattering rates at the optical phonon energies $\hbar\omega_{\lambda}$ are associated with the threshold for optical phonon emission where the carriers have sufficient energy to emit optical phonons.

1. *Effective deformation potentials*

The energy dependence of the first-principles-based scattering rates in Fig. 6 to a high degree resembles that of the analytic expressions for the deformation potential scattering rates in Eqs. (25), (31), and (32). For example, the acoustic and zero-order deformation potential scattering rates are almost constant in the plotted energy range. The first-principles electron-phonon couplings can therefore to a good approximation be described by the simpler isotropic couplings in Eqs. (6) and (7).

The associated *effective* deformation potentials are obtained by fitting their scattering rates for each of the intra and intervalley phonons separately to the first-principles scattering rates. The resulting deformation potential values are summarized in Table I. In analogy with deformation potentials extracted from experimental mobilities, the theoretical deformation potentials represent effective coupling parameters that implicitly account for the anisotropy and the full q dependence of the first-principles electron-phonon couplings. However, as momentum and energy conservation limit phonon scattering to involve phonons in the vicinity of the Γ/K point,[41] the fitting procedure yields deformation potentials in good agreement with the valley-averaged $\mathbf{q} \rightarrow \mathbf{\Gamma/K}$ limiting behavior of the first-principles coupling matrix elements. In case of the zero-order deformation potentials, the sampling of the coupling matrix elements away from the Γ point in the $\mathbf{k}'$ sum of Eq. (30), leads to a deformation potential that is slightly smaller than the Γ point value of the coupling matrix element.

The total scattering rate resulting from the fitted deformation potentials is shown in Fig. 6 to give an almost excellent description of the first-principles scattering rate. The *effective* deformation potentials therefore provide well founded electron-phonon coupling parameters for low-field studies of the mobility with Boltzmann theory.

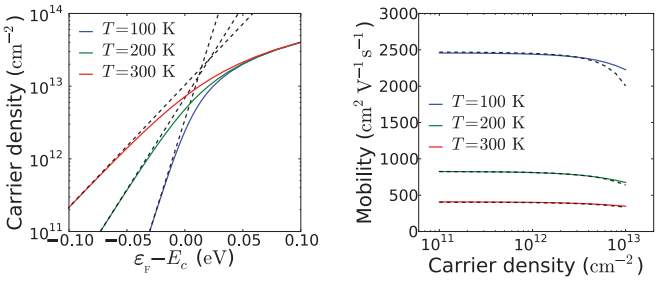

FIG. 7. (Color online) (Left) Carrier density as a function of the Fermi energy for different temperatures. The Fermi energy is measured relative to the conduction band edge E_c. (Right) Mobility as a function of carrier density for the same temperatures. In both plots, the (black) dashed lines show the results obtained with Boltzmann statistics and the relaxation time approximation (only right plot).

B. Mobility

The high density of states in the K, K' valleys of the conduction band, in general, results in nondegenerate carrier distributions in single-layer MoS_2. This is illustrated in the left plot of Fig. 7, which shows the carrier density versus the position of the Fermi level for different temperatures. At room temperature, carrier densities in excess of $\sim 8 \times 10^{12}$ cm^{-2} are needed to introduce the Fermi level into the conduction band and probe the Fermi-Dirac statistics of the carriers. Thus only at the highest reported carrier densities of $n \sim 10^{13}$ cm^{-2},[5] are the carriers degenerate at room temperature. For the lowest temperature $T = 100$ K, the transition to degenerate carriers occurs at a carrier density of $\sim 2 \times 10^{12}$ cm^{-2}. The transition from nondegenerate to degenerate distributions is also illustrated by the discrepancy between the full and dashed lines, which shows the position of the Fermi level obtained with Boltzmann statistics.

The right plot of Fig. 7 shows the phonon-limited drift mobility calculated with the full collision integral as a function of carrier density for the same set of temperatures. The dashed lines represent the results obtained with Boltzmann statistics and the relaxation time approximation using the expressions in Sec. IV for optical phonon scattering. The strong drop in the mobility from $\sim$2450 cm^{2}V^{-1}s^{-1} at $T = 100$ K to $\sim$400 cm^{2}V^{-1}s^{-1} at $T = 300$ K is a consequence of increased phonon scattering at higher temperatures due to, in particular, a higher level of excited optical phonons. The relatively low intrinsic room-temperature mobility of single-layer MoS_2 can be attributed to both significant phonon scattering and the large effective mass of the conduction band. While the mobility decreases strongly with increasing temperature, it is relatively independent on the carrier density. The weak density dependence of the mobility originates from the energy-weighted average in Eq. (20) where the derivative of the Fermi-Dirac distribution changes slowly as a function of carrier density for nondegenerate carriers and only probes the scattering rate near the band edge. Since the Fermi energy is introduced into the band with increasing carrier density, the derivative of the Fermi-Dirac distribution to a larger extent probes the scattering rate at higher energies leading to a decrease of the mobility. This effect is most prominent at $T = 100$ K where the level of degeneracy is larger compared to higher temperatures.

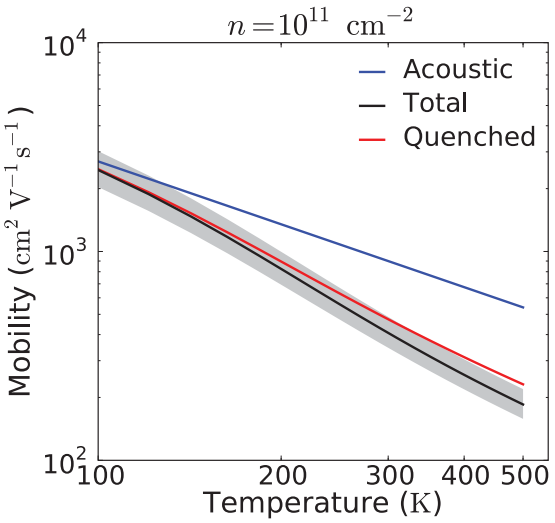

FIG. 8. (Color online) Mobility vs temperature. For comparison, the mobility in the presence of only acoustic deformation potential scattering with the $\mu \sim T^{-1}$ temperature dependence is shown. The (gray) shaded area shows the variation in the mobility associated with a 10% uncertainty in the calculated deformation potentials.

Surprisingly, the relaxation time approximation is seen to work extremely well. The deviation from the full treatment at high carrier densities stems from the assumption of nondegenerate carriers and not the relaxation time approximation. The reason for the good performance of the relaxation-time approximation shall be found in the in-scattering part of the collision integral in the full treatment. As the in-scattering part of the collision integral vanishes for zero-order deformation potential coupling and is small compared to the out-scattering part otherwise, the full collision integral does not differ significantly from the corresponding inverse relaxation time as defined by Eq. (30) for optical phonon scattering. The good performance of the relaxation time approximation therefore seems to be of general validity for the phonon collision integral even in the presence inelastic scattering on optical phonons.

Finally, we study the temperature dependence of the mobility in more detail. In general, room temperature mobilities are to a large extent dominated by optical phonon scattering. This is manifested in a temperature dependence of the mobility which follows a $\mu \sim T^{-\gamma}$ law where the exponent γ depends on the dominating phonon scattering mechanism. For acoustic phonon scattering above the Bloch-Grüneisen temperature, the temperature dependence of the scattering rate in Eq. (25) results in $\gamma = 1$. At higher temperatures where optical phonon scattering starts to dominate, the mobility acquires a stronger temperature dependence with $\gamma > 1$. In this regime, the exponent depends on the optical phonon frequencies and the electron-phonon coupling strength. In an early study of the in-plane mobility of bulk MoS_2,[15] the measured room-temperature exponent of $\gamma \sim 2.6$ was found to be consistent with scattering on the homopolar mode via a zero-order deformation potential.

In Fig. 8, we show the temperature dependence of the mobility at $n = 10^{11}$ cm^{-2} calculated with the full collision integral. For comparison, the mobility limited by acoustic phonon scattering with the $\mu \sim T^{-1}$ temperature dependence is also included. To illustrate the effect of an uncertainty in the calculated deformation potentials, the shaded area shows the variation of the mobility with a change in the deformation potentials of $\pm 10\%$. The calculated room-temperature mobility of $\sim$410 cm^{2}V^{-1}s^{-1} is in fair agreement with the recently reported experimental value of $\sim$200 cm^{2}V^{-1}s^{-1} in the top-gated sample of Ref. 8 where additional scattering mechanisms as, e.g., impurity and surface-optical phonon scattering must be expected to exist. Over the plotted temperature range, the mobility undergoes a transition from being dominated by acoustic phonon scattering at $T = 100$ K to being dominated by optical phonon scattering at higher temperatures with a characteristic exponent of $\gamma > 1$. At room temperature, the mobility follows a temperature dependence with $\gamma = 1.69$ and is dominated by optical phonon scattering through the zero-order deformation potential couplings and the Fröhlich interaction. The first-order deformation potential couplings contribute only marginally. The exponent found here is considerably lower than the above-mentioned exponent of $\gamma \sim 2.6$ for bulk MoS_2, indicating that the electron-phonon coupling in bulk and single-layer MoS_2 differ. Indeed, the transition from an indirect band gap in bulk MoS_2 to a direct band gap in single-layer MoS_2 which shifts the bottom of the conduction band from the valley located along the Γ-K path to the K, K' valleys, could result in a change in the electron-phonon coupling.

In top-gated samples as the one studied in Ref. 8, the sandwiched structure with the MoS_2 layer, located between substrate and gate dielectric, is likely to result in a quenching of the characteristic homopolar mode which is polarized in the direction normal to the layer. To address the consequence of such a quenching, the mobility in the absence of the zero-order deformation potential originating from the coupling to homopolar mode is also shown in Fig. 8. Here, the curve for the quenched case shows a decrease in the characteristic exponent to $\gamma = 1.52$ and an increase in the mobility of $\sim$70 cm^{2}V^{-1}s^{-1} at room temperature. Despite the significant deformation potential of the homopolar mode, the effect of the quenching on the mobility is minor.

VI. DISCUSSIONS AND CONCLUSIONS

Based on our finding for the phonon-limited mobility in single-layer MoS_2, it seems likely that the low experimental mobilities of $\sim$1 cm^{2}V^{-1}s^{-1} reported in Refs. 5,6, and 8 are dominated by other scattering mechanisms such as, e.g., charged impurity scattering. Since a quenching of the out-of-plane homopolar phonon only led to a minor increase in the mobility, the main reason for the increase in the mobility to $\sim$200 cm^{2}V^{-1}s^{-1} observed when depositing a high-κ dielectric on top of the MoS_2 layer in Ref. 8 is therefore likely to be screening of impurities. A comparison of the temperature dependence of the mobility in samples with and without the top-gate structure can help to clarify the extent to which a quenching of optical phonons contributes to the experimentally observed increase in the mobility. With our theoretically predicted room-temperature mobility of $\sim$ 410 cm^{2}V^{-1}s^{-1}, the observed enhancement in the mobility to $\sim$200 cm^{2}V^{-1}s^{-1} induced by the high-κ dielectric, suggests that dielectric engineering[53] is an effective route towards

phonon-limited mobilities in 2D materials via efficient screening of charge impurities.

A rough estimate of the impurity concentrations required to dominate phonon scattering can be inferred from the phonon scattering rate in Fig. 6 which is on the order of $\tau^{-1} \sim 10^{13}$ s^{-1}. The scattering rate is related to the mean-free path λ of the carriers via $\lambda = \tau\langle v\rangle$ where $\langle v\rangle$ is their mean velocity. Using the velocity of the mean-energy carriers in a nondegenerate distribution where $\langle\varepsilon_{\mathbf{k}}\rangle = k_B T$, we find a mean-free path of $\lambda \sim 14$ nm at $T = 300$ K. In order for impurity scattering to dominate, the impurity spacing must be on the order of the phonon mean-free path or smaller. This results in a minimum impurity concentration of $\sim 5 \times 10^{11}$ cm^{-2} in order to dominate phonon scattering. The high value of the estimated impurity concentration needed to dominate phonon scattering is in agreement with the experimental observation that low-mobility single-layer MoS_2 samples are heavily doped semiconductors.[5]

As discussed in Sec. II, independent GW quasiparticle calculations[55,56] suggest that the ordering of the valleys at the bottom of the conduction band might not be as clear as predicted by DFT. If this is the case, the satellite valleys inside the Brillouin zone must also be taken into account in the solution of Boltzmann equation. For a valley separation on the order of the corresponding intervalley phonon energies, additional scattering on the intervalley phonons is introduced. Together with the larger average effective electron mass $m^* \sim 0.8\ m_e$ of the satellite valleys, the intervalley scattering channels will result in mobilities below the values predicted here. In case of a complete valley inversion the carriers will reside in the satellite valleys instead of K, K' valleys. For this case, we have calculated the mobility with the prescription used for the mobility in the K, K' valleys. Surprisingly, we find that the scattering rate in the satellite valleys is dominated by intravalley acoustic phonon scattering and is on the order of $\sim 10^{16}-10^{17}$ s^{-1}. The extremely large scattering rate in the satellite valleys stems from a strong coupling to the acoustic phonons that bears close resemblance to that of piezoelectric coupling, i.e., with a strongly anisotropic and q-independent coupling matrix element $M_q \sim$ const.[57] The resulting mobility of <1 $cm^2V^{-1}s^{-1}$ is orders of magnitude smaller than the mobility in the K, K' valleys, why experimental mobilities on the order of 200 $cm^2V^{-1}s^{-1}$ must be attributed to carriers in K, K' valleys.

In conclusion, we have used a first-principles approach to establish the strength and nature of the electron-phonon interaction and calculate the intrinsic phonon-limited mobility in single-layer MoS_2. The calculated room-temperature mobility of 410 $cm^2V^{-1}s^{-1}$ is to a large extent dominated by optical deformation potential scattering on the intravalley homopolar and intervalley LO phonons as well as polar optical scattering on the intravalley LO phonon via the Fröhlich interaction. The mobility follows a $\mu \sim T^{-1.69}$ temperature dependence at room temperature characteristic of optical phonon scattering. A quenching of the homopolar mode, which is likely to occur in top-gated samples, results in a change of the exponent in the temperature dependence of the mobility to 1.52. With effective masses, phonons, and measured mobilities in other semiconducting metal dichalcogenides being similar to those of MoS_2,[15,24] room-temperature mobilities of the same order of magnitude can be expected in their single-layer forms.

ACKNOWLEDGMENTS

The authors would like to thank O. Hansen, A.-P. Jauho, and J. J. Mortensen for illuminating discussions and comments on the manuscript. K.K. has been partially supported by the Center on Nanostructuring for Efficient Energy Conversion (CNEEC) at Stanford University, an Energy Frontier Research Center funded by the US Department of Energy, Office of Science, Office of Basic Energy Sciences under Award Number DE-SC0001060. CAMD is supported by the Lundbeck Foundation.

APPENDIX A: FIRST-PRINCIPLES CALCULATION OF THE ELECTRON-PHONON INTERACTION

The first-principles scheme for the calculation of the electron-phonon interaction used in this work is outlined in the following. Contrary to other first-principles approaches for the calculation of the electron-phonon interaction that are based on pseudopotentials,[43–45,58] the present approach is based on the projector-augmented wave (PAW) method[59] and is implemented in the GPAW DFT package.[26–28]

Within the adiabatic approximation for the electron-phonon interaction, the electron-phonon coupling matrix elements for the phonon $\mathbf{q}\lambda$ and Bloch state $\mathbf{k}$ can be expressed as

$$g^{\lambda}_{\mathbf{kq}} = \sqrt{\frac{\hbar}{2MN\omega_{\mathbf{q}\lambda}}} \sum_{\alpha} \langle \mathbf{k}+\mathbf{q}|\hat{\mathbf{e}}^{\mathbf{q}\lambda}_{\alpha} \cdot \nabla^{\mathbf{q}}_{\alpha} V(\mathbf{r})|\mathbf{k}\rangle, \quad \text{(A1)}$$

where N is the number of unit cells, M is an appropriately defined effective mass, $\omega_{\mathbf{q}\lambda}$ is the phonon frequency, and the $\mathbf{q}$-dependent derivative of the effective potential for a given atom α is defined by

$$\nabla^{\mathbf{q}}_{\alpha} V(\mathbf{r}) = \sum_{l} e^{i\mathbf{q}\cdot\mathbf{R}_l} \nabla_{\alpha l} V(\mathbf{r}), \quad \text{(A2)}$$

where the sum is over unit cells in the system and $\nabla_{\alpha l} V$ is the gradient of the potential with respect to the position of atom α in cell $\mathbf{R}_l$. The polarization vectors $\hat{\mathbf{e}}_{\mathbf{q}\lambda}$ of the phonons appearing in Eq. (A1) are normalized according to $\sum_{\alpha}(M_{\alpha}/M)|\hat{\mathbf{e}}^{\mathbf{q}\lambda}_{\alpha}|^2 = 1$.

In order to evaluate the matrix element in Eq. (A1), the Bloch states are expanded in LCAO basis orbitals $|i\mathbf{R}_n\rangle$, where $i = (\alpha,\mu)$ is a composite index for atomic site and orbital index and $\mathbf{R}_n$ is the lattice vector to the n'th unit cell. In the LCAO basis, the Bloch states are expanded as $|\mathbf{k}\rangle = \sum_i c^{\mathbf{k}}_i |i\mathbf{k}\rangle$ where

$$|i\mathbf{k}\rangle = \frac{1}{N} \sum_{n} e^{i\mathbf{k}\cdot\mathbf{R}_n} |i\mathbf{R}_n\rangle \quad \text{(A3)}$$

are Bloch sums of the localized orbitals. Inserting the Bloch sum expansion of the Bloch states in the matrix element in Eq. (A1), the matrix element can be written

$$\begin{aligned}
&\langle \mathbf{k}+\mathbf{q}|\hat{\mathbf{e}}_{\mathbf{q}\lambda} \cdot \nabla_{\mathbf{q}} V(\mathbf{r})|\mathbf{k}\rangle \\
&\quad = \sum_{ij} c^*_i c_j \langle i\mathbf{k}+\mathbf{q}|\hat{\mathbf{e}}_{\mathbf{q}\lambda} \cdot \nabla_{\mathbf{q}} V(\mathbf{r})|j\mathbf{k}\rangle \\
&\quad = \frac{1}{N^2} \sum_{ij} c^*_i c_j \sum_{lmn} e^{i(\mathbf{k}+\mathbf{G})\cdot(\mathbf{R}_n-\mathbf{R}_m) - i\mathbf{q}\cdot(\mathbf{R}_m-\mathbf{R}_l)} \\
&\quad \times \langle i\mathbf{R}_m|\hat{\mathbf{e}}_{\mathbf{q}\lambda} \cdot \nabla_l V(\mathbf{r})|j\mathbf{R}_n\rangle, \quad \text{(A4)}
\end{aligned}$$

where the $\mathbf{k}$ labels on the expansion coefficients have been discarded for brevity. The phase factor from the reciprocal lattice vector $\mathbf{G}$ can be neglected since $\mathbf{R}_n \cdot \mathbf{G} = 2\pi N$. By exploiting the translational invariance of the crystal, the matrix elements can be obtained from the gradient in the primitive cell as

$$\begin{aligned}&\langle i\mathbf{R}_m|\hat{\mathbf{e}}_{\mathbf{q}\lambda}\cdot\nabla_l V(\mathbf{r})|j\mathbf{R}_n\rangle\\&\quad=\langle i\mathbf{R}_m-\mathbf{R}_l|\hat{\mathbf{e}}_{\mathbf{q}\lambda}\cdot\nabla_0 V(\mathbf{r})|j\mathbf{R}_n-\mathbf{R}_l\rangle\end{aligned}\tag{A5}$$

by performing the change of variables $\mathbf{r}' = \mathbf{r} - \mathbf{R}_l$ in the integration. Inserting in Eq. (A4) and changing the summing variables to $\mathbf{R}_m - \mathbf{R}_l$ and $\mathbf{R}_n - \mathbf{R}_l$, we find for the matrix element

$$\begin{aligned}&\langle\mathbf{k}+\mathbf{q}|\hat{\mathbf{e}}_{\mathbf{q}\lambda}\cdot\nabla_{\mathbf{q}}V(\mathbf{r})|\mathbf{k}\rangle\\&\quad=\frac{1}{N^2}\sum_{ij}c_i^*c_j\sum_{lmn}e^{i\mathbf{k}\cdot(\mathbf{R}_n-\mathbf{R}_m)-i\mathbf{q}\cdot\mathbf{R}_m}\\&\qquad\times\langle i\mathbf{R}_m|\hat{\mathbf{e}}_{\mathbf{q}\lambda}\cdot\nabla_0 V(\mathbf{r})|j\mathbf{R}_n\rangle\\&\quad=\frac{1}{N}\sum_{ij}c_i^*c_j\sum_{mn}e^{i\mathbf{k}\cdot(\mathbf{R}_n-\mathbf{R}_m)-i\mathbf{q}\cdot\mathbf{R}_m}\\&\qquad\times\langle i\mathbf{R}_m|\hat{\mathbf{e}}_{\mathbf{q}\lambda}\cdot\nabla_0 V(\mathbf{r})|j\mathbf{R}_n\rangle.\end{aligned}\tag{A6}$$

Here, the sum over k in the first equality produces a factor of N. The result for the matrix element in Eq. (A6) is similar to the matrix element reported in Eq. (22) of Ref. 58 where a Wannier basis was used instead of the LCAO basis.

From the last equality in Eq. (A6), the procedure for a supercell-based evaluation of the matrix element has emerged. The matrix element in the last equality involves the gradients of the effective potential $\nabla_0 V$ with respect to atomic displacement in the reference cell at $\mathbf{R}_0$. These can be obtained using a finite-difference approximation for the gradient where the individual components are obtained as

$$\frac{\partial V}{\partial R_{\alpha i}}=\frac{V_{\alpha i}^{+}(\mathbf{r})-V_{\alpha i}^{-}(\mathbf{r})}{2\delta}.\tag{A7}$$

Here, $V_{\alpha i}^{\pm}$ denotes the effective potential with atom α located at $\mathbf{R}_\alpha$ in the reference cell displaced by $\pm\delta$ in direction $i = x,y,z$. The calculation of the gradient thus amounts to carrying out self-consistent calculations for six displacements of each atom in the primitive unit cell. Having obtained the gradients of the effective potential, the matrix elements in the LCAO basis of the supercell must be calculated and the sums over unit cells and atomic orbitals in Eq. (A6) can be evaluated.

In general, the matrix elements of the electron-phonon interaction must be converged with respect to the supercell size and the LCAO basis. In particular, since the supercell approach relies on the gradient of the effective potential going to zero at the supercell boundaries, the supercell must be chosen large enough that the potential at the boundaries is negligible. For polar materials where the coupling to the polar LO phonon is long-ranged in nature, a correct description of the coupling can only be obtained for phonon wave vectors corresponding to wavelengths smaller than the supercell size. Large supercells are therefore required to capture the long-wavelength limit of the coupling constant (see, e.g., main text).

1. PAW details

In the PAW method, the effective single-particle DFT Hamiltonian is given by

$$H=-\frac{1}{2}\nabla^2+v_{\mathrm{eff}}(\mathbf{r})+\sum_{\alpha}\sum_{i_1 i_2}|\tilde{p}_{i_1}^{\alpha}\rangle\Delta H_{i_1 i_2}^{\alpha}\langle\tilde{p}_{i_2}^{\alpha}|,\tag{A8}$$

where the first term is the kinetic energy, v_{eff} is the effective potential containing contributions from the atomic potentials and the Hartree and exchange-correlation potentials, and the last term is the nonlocal part including the atom-centered projector functions $\tilde{p}_i^{\alpha}(\mathbf{r})$ and the atomic coefficients $\Delta H_{i_1 i_2}^{\alpha}$. In contrast to pseudopotential methods where the atomic coefficients are constants, they depend on the density and thereby also on the atomic positions in the PAW method.

The diagonal matrix elements (i.e., $\mathbf{q} = \mathbf{0}$) in Eq. (A4) correspond to the first-order variation in the band energy $\varepsilon_{\mathbf{k}}$ upon an atomic displacement in the normal mode direction $\hat{\mathbf{e}}_{\mathbf{q}\lambda}$. Together with the matrix elements for $\mathbf{q} \neq \mathbf{0}$, these can be obtained from the gradient of the PAW Hamiltonian with respect to atomic displacements. The derivative of (A8) with respect to a displacement of atom α in direction i results in the following four terms

$$\begin{aligned}\frac{\partial H}{\partial R_{\alpha i}}=&\frac{\partial v_{\mathrm{eff}}}{\partial R_{\alpha i}}+\sum_{i_1,i_2}\left[\left|\frac{\partial\tilde{p}_{i_1}^{\alpha}}{\partial R_{\alpha i}}\right\rangle\Delta H_{i_1 i_2}^{\alpha}\langle\tilde{p}_{i_2}^{\alpha}|\right.\\&\left.+|\tilde{p}_{i_1}^{\alpha}\rangle\Delta H_{i_1 i_2}^{\alpha}\left\langle\frac{\partial\tilde{p}_{i_2}^{\alpha}}{\partial R_{\alpha i}}\right|+|\tilde{p}_{i_1}^{\alpha}\rangle\frac{\partial\Delta H_{i_1 i_2}^{\alpha}}{\partial R_{\alpha i}}\langle\tilde{p}_{i_2}^{\alpha}|\right].\end{aligned}\tag{A9}$$

While the gradient of the projector functions in the first and second terms inside the square brackets can be evaluated analytically, the gradients of the effective potential and the projector coefficients in the last term are obtained using the finite-difference approximation in Eq. (A7).

Once the gradient of the PAW Hamiltonian has been obtained, the matrix elements in Eq. (A4) can be obtained. Under the assumption that the smooth pseudo-Bloch wave functions $\tilde{\psi}_{\mathbf{k}}$ from the PAW formalism is a good approximation to the true quasiparticle wave function, the matrix element follows as

$$\langle\mathbf{k}+\mathbf{q}|\hat{\mathbf{e}}_{\mathbf{q}\lambda}\cdot\nabla_{\mathbf{q}}V(\mathbf{r})|\mathbf{k}\rangle=\langle\tilde{\psi}_{\mathbf{k}+\mathbf{q}}|\hat{\mathbf{e}}_{\mathbf{q}\lambda}\cdot\nabla_{\mathbf{q}}H|\tilde{\psi}_{\mathbf{k}}\rangle,\tag{A10}$$

where $\nabla_{\mathbf{q}}H$ is given in Eq. (A2). With the pseudo-wavefunction expanded in an LCAO basis, the matrix element is evaluated following Eq. (A6).

In order to verify the calculated matrix elements, we have carried out self-consistent calculations of the variation in the band energies with respect to atomic displacements along the phonon normal mode. For the coupling to the Γ-point homopolar phonon in single-layer MoS_2, we find that the calculated matrix element of 4.8 eV/Å agrees with the self-consistently calculated value to within 0.1 eV/Å.

As the matrix elements of the electron-phonon interaction are sensitive to the behavior of the potential and wave functions in the vicinity of the atomic cores, variations in electron-phonon couplings obtained with different pseudopotential approximations can be expected. We have confirmed this via self-consistent calculations of the band energy variations, which showed that the coupling to the homopolar Γ-point phonon increases by 0.3 eV/Å compared to the PAW value when using norm-conserving Hartwigsen-Goedecker-Hutter (HGH) pseudo potentials.

APPENDIX B: FRÖHLICH INTERACTION IN 2D MATERIALS

In the long-wavelength limit, the lattice vibration of the polar LO mode gives rise to a macroscopic polarization that couples to the charge carriers. In three-dimensional bulk systems, the coupling strength is given by Eq. (8), which diverges as $1/q$. Using dielectric continuum models, the coupling has been studied for confined carriers and LO phonons in semiconductor heterostructures.[46,47] For atomically thin materials, macroscopic dielectric models are inappropriate. Using microscopic approach based on the atomic Born effective charges Z^*, an analytical functional form for the Fröhlich interaction in 2D materials is here derived.

1. Polarization field and potential

In two-dimensional materials, the polarization from the lattice vibration of the polar LO phonon is oriented along the plane of the layer. It can be expressed in terms of the relative displacement $\mathbf{u_q}$ of the unit cell atoms as

$$\mathbf{P_q}(z) = \frac{Z^*}{\varepsilon_\infty A}\mathbf{u_q} f_\mathbf{q}(z), \tag{B1}$$

where $\mathbf{q}$ is the two-dimensional phonon wave vector, ε_∞ is the optical dielectric constant, Z^* is the Born effective charge of the atoms (assumed to be of equal magnitude for all atoms), and $f_\mathbf{q}$ describes the profile of the polarization in the direction perpendicular (here the z direction) to the layer. The associated polarization charge $\rho = -\nabla\cdot\mathbf{P}$ is given by $\rho_\mathbf{q} = -i\mathbf{q}\cdot\mathbf{P_q}$. The resulting scalar potential that couples to the carriers follows from Poisson's equation. Fourier transforming in all three directions, Poisson's equation takes the form

$$(q^2+k^2)\phi_\mathbf{q}(k) = -i\frac{Z^*}{\epsilon_0\varepsilon_\infty A}\mathbf{q}\cdot\mathbf{u_q} f_\mathbf{q}(k), \tag{B2}$$

where k is the Fourier variable in the direction perpendicular to the plane of the layer and $\mathbf{q} \parallel \mathbf{u_q}$ for the LO phonon.

In 2D materials, the z profile of the polarization field can to a good approximation be described by a δ function, i.e.,

$$f_\mathbf{q}(z) = \delta(z). \tag{B3}$$

Inserting the Fourier transform $f_\mathbf{q}(k) = 1$ in Eq. (B2), we find for the potential

$$\begin{aligned}\phi_\mathbf{q}(z) &= -i\frac{Z^* u_\mathbf{q}}{\epsilon_0\varepsilon_\infty A}\int dk\; e^{ikz} f_\mathbf{q}(k)\frac{q}{q^2+k^2}\\ &= -i\frac{Z^* u_\mathbf{q}}{\epsilon_0\varepsilon_\infty A}e^{-q|z|}\end{aligned} \tag{B4}$$

that, in agreement with the findings of Refs. 46 and 47, does not diverge in the long-wavelength limit.

2. Electron-phonon interaction

In three-dimensional bulk systems, the q dependence of the Fröhlich interaction is given entirely by the $1/q$ divergence of the potential associated with the lattice vibration of the polar LO phonon. However, in two dimensions, the interaction follows by integrating the potential with the square of the envelope function $\chi(z)$ of the electronic Bloch state. Hence, the Fröhlich interaction is given by the matrix element

$$g_{\mathrm{LO}}(q) = \int dz\; \chi^*(z)\phi_\mathbf{q}(z)\chi(z). \tag{B5}$$

For simplicity, we here assume a Gaussian profile for the envelope function

$$\chi(z) = \frac{1}{\pi^{1/4}\sqrt{\sigma}}e^{-z^2/2\sigma^2}, \tag{B6}$$

where σ denotes the effective width of the electronic Bloch function. With this approximation for the envelope function, the Fröhlich interaction becomes

$$\begin{aligned}g_{\mathrm{LO}}(q) &= g_{\mathrm{Fr}}\, e^{q^2\sigma^2/4}\mathrm{erfc}(q\sigma/2)\\ &\approx g_{\mathrm{Fr}}\,\mathrm{erfc}(q\sigma/2),\end{aligned} \tag{B7}$$

where g_{Fr} is the Fröhlich coupling constant, erfc is the complementary error function, and the last equality holds in the long-wavelength limit where $q^{-1} \gg \sigma$. As shown in Fig. 5 in the main text, this functional form for the Fröhlich interaction gives a perfect fit to the calculated electron-phonon coupling for the polar LO mode.

APPENDIX C: EVALUATION OF THE INELASTIC COLLISION INTEGRAL

Following Eq. (26) in the main text, the inelastic collision integral for scattering on optical phonons is split up in separate out- and in-scattering contributions,

$$I'_{\mathrm{inel}}[\phi_k] = I'^{\mathrm{out}}_{\mathrm{inel}}[\phi_k] + I'^{\mathrm{in}}_{\mathrm{inel}}[\phi_k], \tag{C1}$$

which are given by Eqs. (27) and (29), respectively. With the assumption of dispersionless optical phonons, the Fermi-Dirac and Bose-Einstein distribution functions do not depend on the phonon wave vector and can thus be taken outside the $\mathbf{q}$ sum.

The out-scattering part of the collision integral then takes the form

$$I'^{\mathrm{out}}_{\mathrm{inel}}[\phi_k] = -\frac{2\pi}{\hbar}\frac{\phi_k}{1-f^0_\mathbf{k}}\times\left[N^0_\lambda\left(1-f^0_{\mathbf{k}+\mathbf{q}}\right)\sum_\mathbf{q}|g_\mathbf{q}|^2\delta(\varepsilon_{\mathbf{k}+\mathbf{q}}-\varepsilon_\mathbf{k}-\hbar\omega_\lambda) + \left(1+N^0_\lambda\right)\left(1-f^0_{\mathbf{k}-\mathbf{q}}\right)\sum_\mathbf{q}|g_\mathbf{q}|^2\delta(\varepsilon_{\mathbf{k}-\mathbf{q}}-\varepsilon_\mathbf{k}+\hbar\omega_\lambda)\right]. \tag{C2}$$

For the in-scattering part, the additional $\cos\theta_{\mathbf{k},\mathbf{k}\pm\mathbf{q}}$ factor is rewritten as

$$\cos\theta_{\mathbf{k},\mathbf{k}\pm\mathbf{q}} = \frac{k\pm q\cos\theta_{\mathbf{k},\mathbf{q}}}{k\sqrt{1\pm\frac{\hbar\omega_\lambda}{\varepsilon_\mathbf{k}}}}, \tag{C3}$$

leading to the following general form of the in-scattering part of the collision integral:

$$I'^{\text{in}}_{\text{inel}}[\phi_k] = \frac{2\pi}{\hbar}\frac{1}{1-f^0_{\mathbf{k}}}\Bigg[N^0_\lambda\big(1-f^0_{\mathbf{k}+\mathbf{q}}\big)\frac{\phi_{k+q}}{k\sqrt{1+\frac{\hbar\omega_\lambda}{\varepsilon_{\mathbf{k}}}}}\times\sum_{\mathbf{q}}|g_{\mathbf{q}}|^2(k+q\cos\theta_{\mathbf{k},\mathbf{q}})\delta(\varepsilon_{\mathbf{k}+\mathbf{q}}-\varepsilon_{\mathbf{k}}-\hbar\omega_\lambda)$$
$$+\big(1+N^0_\lambda\big)\big(1-f^0_{\mathbf{k}-\mathbf{q}}\big)\frac{\phi_{k-q}}{k\sqrt{1-\frac{\hbar\omega_\lambda}{\varepsilon_{\mathbf{k}}}}}\times\sum_{\mathbf{q}}|g_{\mathbf{q}}|^2(k-q\cos\theta_{\mathbf{k},\mathbf{q}})\times\delta(\varepsilon_{\mathbf{k}-\mathbf{q}}-\varepsilon_{\mathbf{k}}+\hbar\omega_\lambda)\Bigg]. \tag{C4}$$

This depends on the deviation function in $\phi_{k\pm q}\equiv\phi(\varepsilon_{\mathbf{k}}\pm\hbar\omega_\lambda)$ and thus couples the deviation function at the initial energy $\varepsilon_{\mathbf{k}}$ of the carrier to that at $\varepsilon_{\mathbf{k}}\pm\hbar\omega_\lambda$. The two terms inside the square brackets account for emission and absorption out of the state $\mathbf{k}\pm\mathbf{q}$ and into the state $\mathbf{k}$, respectively.

1. Integration over q

The in- and out-scattering contributions to the inelastic part of the collision integral in Eqs. (C2) and (C4) can be written on the general form

$$I'^{\text{in/out}}_{\text{inel}}(\mathbf{k}) = \sum_{\mathbf{q}} f(q)\delta(\varepsilon_{\mathbf{k}\pm\mathbf{q}}-\varepsilon_{\mathbf{k}}\mp\hbar\omega_{\mathbf{q}\lambda}), \tag{C5}$$

where the function f accounts for the q-dependent functions inside the $\mathbf{q}$ sum. The conservation of energy and momentum in a scattering event is secured by the δ function entering the collision integral.

Following the procedure outlined in Ref. 15, the integral over q resulting from the $\mathbf{q}$ sum in the collision integral is evaluated using the following property of the δ function,

$$\int dq\ F(q)\delta[g(q)] = \sum_n \frac{F(q_n)}{|g'(q_n)|}. \tag{C6}$$

Here, $F(q)=qf(q)$ and q_n are the roots of g. Rewriting the argument of the δ function in Eq. (C5) as

$$\begin{aligned}\varepsilon_{\mathbf{k}\pm\mathbf{q}}-\varepsilon_{\mathbf{k}}\mp\hbar\omega_{\mathbf{q}\lambda} &= \frac{\hbar^2(\mathbf{k}\pm\mathbf{q})^2}{2m^*}-\frac{\hbar^2k^2}{2m^*}\mp\hbar\omega_{\mathbf{q}\lambda}\\ &= \frac{\hbar^2}{2m^*}\left(q^2\pm2kq\cos\theta_{\mathbf{k},\mathbf{q}}\mp\frac{2m^*\omega_{\mathbf{q}\lambda}}{\hbar}\right)\\ &\equiv \frac{\hbar^2}{2m^*}g(q),\end{aligned} \tag{C7}$$

we get

$$I'(\mathbf{k}) = \frac{A}{(2\pi)^2}\int d\theta_{\mathbf{k},\mathbf{q}}\,\frac{2m^*}{\hbar^2}\sum_n\frac{q_nf(q_n)}{|g'(q_n)|}. \tag{C8}$$

Depending on the q dependence of the phonon frequency, different solutions for the roots q_n result.

a. Dispersionless optical phonons

With the assumption of dispersionless optical phonons, i.e., $\omega_{\mathbf{q}\lambda}=\omega_\lambda$, the roots of g in Eq. (C7) become

$$q/k = \mp\cos\theta_{\mathbf{k},\mathbf{q}}\pm\sqrt{\cos^2\theta_{\mathbf{k},\mathbf{q}}\pm\frac{\hbar\omega_\lambda}{\varepsilon_{\mathbf{k}}}} \tag{C9}$$

for absorption (upper sign in the first and last terms) and emission (lower sign in the first and last terms), respectively.

For absorption, there is only one positive root q^a_+ given by the plus sign in front of the square root,

$$q^a_+ = -k\cos\theta_{\mathbf{k},\mathbf{q}}+k\sqrt{\cos^2\theta_{\mathbf{k},\mathbf{q}}+\frac{\hbar\omega_\lambda}{\varepsilon_{\mathbf{k}}}} \tag{C10}$$

where all values of $\theta_{\mathbf{k},\mathbf{q}}$ are allowed. The absorption terms in the collision integral then become

$$I'_a(\mathbf{k}) = \frac{A}{(2\pi)^2}\int_0^{2\pi}d\theta_{\mathbf{k},\mathbf{q}}\,\frac{m^*}{k\hbar^2}\frac{q^a_+f(q^a_+)}{\sqrt{\cos^2\theta_{\mathbf{k},\mathbf{q}}+\frac{\hbar\omega_\lambda}{\varepsilon_{\mathbf{k}}}}}. \tag{C11}$$

In the case of phonon emission, both possible roots in Eq. (C9)

$$q^e_\pm = k\cos\theta_{\mathbf{k},\mathbf{q}}\pm k\sqrt{\cos^2\theta_{\mathbf{k},\mathbf{q}}-\frac{\hbar\omega_\lambda}{\varepsilon_{\mathbf{k}}}} \tag{C12}$$

can take on positive values. However, the minus sign inside the square root restricts the allowed values of the integration angle to the range $\theta_{\mathbf{k},\mathbf{q}}\leqslant\theta_0=\arccos(\hbar\omega_\lambda/\varepsilon_{\mathbf{k}})^{1/2}$. Furthermore, in order to secure a positive argument to the square root, the electron energy must be larger than the phonon energy, $\varepsilon_{\mathbf{k}}>\hbar\omega_\lambda$. Hence, the emission terms can be obtained as

$$I'_e(\mathbf{k}) = \frac{A}{(2\pi)^2}\Theta(\varepsilon_{\mathbf{k}}-\hbar\omega_\lambda)\times\int_{-\theta_0}^{\theta_0}d\theta_{\mathbf{k},\mathbf{q}}\,\frac{m^*}{k\hbar^2}\frac{q^e_+f(q^e_+)+q^e_-f(q^e_-)}{\sqrt{\cos^2\theta_{\mathbf{k},\mathbf{q}}-\frac{\hbar\omega_\lambda}{\varepsilon_{\mathbf{k}}}}}. \tag{C13}$$

In the following section, analytic expressions for collision integral in the case of zero- and first-order optical deformation potential coupling are given. For the 2D Fröhlich interaction in Eq. (9), the integration over θ cannot be reduced to a simple analytic form and must therefore evaluated numerically.

2. Collision integral for optical deformation potential scattering

a. Zero-order deformation potential

For the zero-order deformation potential coupling in Eq. (7), the θ integration in the out-scattering part of the collision integral yields a factor of 2π resulting in the following expression for the out-scattering part:

$$I'^{\text{out}}_{\text{inel}}[\phi_k] = -\frac{m^* D_\lambda^2}{2\hbar^2\rho\omega_\lambda}\frac{\phi_k}{1-f^0_{\mathbf{k}}} \times \left[\left(1-f^0_{\mathbf{k}+\mathbf{q}}\right) + \left(1-f^0_{\mathbf{k}-\mathbf{q}}\right)e^{\hbar\omega_\lambda/k_BT}\Theta(\varepsilon_{\mathbf{k}}-\hbar\omega_\lambda)\right]N^0_\lambda. \quad \text{(C14)}$$

For the in-scattering part, the q independence of the deformation potential results in a vanishing $\mathbf{q}$ sum and the in-scattering contribution is zero, i.e.,

$$I'^{\text{in}}_{\text{inel}}[\phi_k] = 0. \quad \text{(C15)}$$

b. First-order deformation potential

For first-order deformation potentials, we find for the out-scattering part,

$$I'^{\text{out}}_{\text{inel}}[\phi_k] = -\frac{m^{*2}\Xi_\lambda^2}{\hbar^4\rho\omega_\lambda}\frac{\phi_k}{1-f^0_{\mathbf{k}}} \times \left[\left(1-f^0_{\mathbf{k}+\mathbf{q}}\right)(2\varepsilon_{\mathbf{k}}+\hbar\omega_\lambda) + \left(1-f^0_{\mathbf{k}-\mathbf{q}}\right)(2\varepsilon_{\mathbf{k}}-\hbar\omega_\lambda) \times e^{\hbar\omega_\lambda/k_BT}\Theta(\varepsilon_{\mathbf{k}}-\hbar\omega_\lambda)\right]N^0_\lambda. \quad \text{(C16)}$$

For the in-scattering part, the result for the first and second terms inside the square brackets in Eq. (C4) is

$$I'^{\text{in}}_{\text{inel}}[\phi_k] = -\frac{m^{*2}\Xi_\lambda^2}{\hbar^4\rho\omega_\lambda}\frac{1-f^0_{\mathbf{k}+\mathbf{q}}}{1-f^0_{\mathbf{k}}}\frac{\phi_{k+q}}{\sqrt{1+\frac{\hbar\omega_\lambda}{\varepsilon_{\mathbf{k}}}}}(\varepsilon_{\mathbf{k}}+\hbar\omega_\lambda)N^0_\lambda \quad \text{(C17)}$$

and

$$I'^{\text{in}}_{\text{inel}}[\phi_k] = -\frac{m^{*2}\Xi_\lambda^2}{\hbar^4\rho\omega_\lambda}\frac{1-f^0_{\mathbf{k}-\mathbf{q}}}{1-f^0_{\mathbf{k}}}\frac{\phi_{k-q}}{\sqrt{1-\frac{\hbar\omega_\lambda}{\varepsilon_{\mathbf{k}}}}}\Theta(\varepsilon_{\mathbf{k}}-\hbar\omega_\lambda)(\varepsilon_{\mathbf{k}}-\hbar\omega_\lambda)\left(1+N^0_\lambda\right) \times \frac{1}{\pi}\left(\frac{\pi}{2}+\arccos\sqrt{\frac{\hbar\omega_\lambda}{\varepsilon_{\mathbf{k}}}}+\arcsin\sqrt{\frac{\hbar\omega_\lambda}{\varepsilon_{\mathbf{k}}}}\right), \quad \text{(C18)}$$

which account for absorption and emission, respectively.

*cosby@fys.ku.dk

[1] A. K. Geim and K. S. Novoselov, Nat. Mater. **6**, 183 (2007).
[2] A. H. C. Neto, F. Guinea, N. M. R. Peres, K. S. Novoselov, and A. K. Geim, Rev. Mod. Phys. **81**, 109 (2009).
[3] S. D. Sarma, S. Adam, E. H. Hwang, and E. Rossi, Rev. Mod. Phys. **83**, 407 (2011).
[4] A. H. C. Neto and K. Novoselov, Rep. Prog. Phys. **74**, 082501 (2011).
[5] K. S. Novoselov, D. Jiang, F. Schedin, T. J. Booth, V. V. Khotkevich, S. V. Morozov, and A. K. Geim, PNAS **102**, 10451 (2005).
[6] A. Ayari, E. Cobas, O. Ogundadegbe, and M. S. Fuhrer, J. Appl. Phys. **101**, 014507 (2007).
[7] H. S. S. R. Matte, A. Gomathi, A. K. Manna, D. J. Late, R. Datta, S. K. Pati, and C. N. R. Rao, Angew. Chem. **122**, 4153 (2010).
[8] B. Radisavljevic, A. Radenovic, J. Brivio, V. Giacometti, and A. Kis, Nat. Nanotechnology **6**, 147 (2011).
[9] C. Lee, H. Yan, L. E. Brus, T. F. Heinz, J. Hone, and S. Ryu, ACS Nano **4**, 2695 (2010).
[10] K. F. Mak, C. Lee, J. Hone, J. Shan, and T. F. Heinz, Phys. Rev. Lett. **105**, 136805 (2010).
[11] T. Korn, S. Heydrich, M. Hirmer, J. Schmutzler, and C. Schüller, Appl. Phys. Lett. **99**, 102109 (2011).
[12] H. Liu and P. D. Ye, e-print arXiv:1112.4397v1 (2011).
[13] A. Splendiani, L. Sun, Y. Zhang, T. Li, J. Kim, C.-Y. Chim, G. Galli, and F. Wang, Nano Lett. **10**, 1271 (2010).
[14] Y. Yoon, K. Ganapathi, and S. Salahuddin, Nano. Lett. **11**, 3768 (2011).
[15] R. Fivaz and E. Mooser, Phys. Rev. **163**, 743 (1967).
[16] E. H. Hwang and S. Das Sarma, Phys. Rev. B **77**, 235437 (2008).
[17] T. Kawamura and S. Das Sarma, Phys. Rev. B **42**, 3725 (1990).
[18] E. H. Hwang, S. Adam, and S. Das Sarma, Phys. Rev. Lett. **98**, 186806 (2007).
[19] K. Nomura and A. H. MacDonald, Phys. Rev. Lett. **98**, 076602 (2007).
[20] J.-H. Chen, C. Jang, S. Xiao, M. Ishigami, and M. S. Fuhrer, Nat. Nanotechnology **3**, 206 (2008).
[21] A. Konar, T. Fang, and D. Jena, Phys. Rev. B **82**, 115452 (2010).
[22] X. Li, E. A. Barry, J. M. Zavada, M. B. Nardelli, and K. W. Kim, Appl. Phys. Lett. **97**, 232405 (2010).
[23] J. Heo, H. J. Chung, S.-H. Lee, H. Yang, D. H. Seo, J. K. Shin, U.-In. Chung, S. Seo, E. H. Hwang, and S. Das Sarma, Phys. Rev. B **84**, 035421 (2011).
[24] R. C. Fivaz, Nuovo Cimento **63 B**, 10 (1969).
[25] P. Schmid, Nuovo Cimento **21 B**, 258 (1974).
[26] J. J. Mortensen, L. B. Hansen, and K. W. Jacobsen, Phys. Rev. B **71**, 035109 (2005).
[27] A. H. Larsen, M. Vanin, J. J. Mortensen, K. S. Thygesen, and K. W. Jacobsen, Phys. Rev. B **80**, 195112 (2009).
[28] J. Enkovaara *et al.*, J. Phys. Condens. Matter **22**, 253202 (2010).
[29] S. Lebègue and O. Eriksson, Phys. Rev. B **79**, 115409 (2009).
[30] S. W. Han, H. Kwon, S. K. Kim, S. Ryu, W. S. Yun, D. H. Kim, J. H. Hwang, J.-S. Kang, J. Baik, H. J. Shin, and S. C. Hong, Phys. Rev. B **84**, 045409 (2011).
[31] D. Alfé, Comput. Phys. Commun. **180**, 2622 (2009).

[32]A. Molina-Sánchez and L. Wirtz, Phys. Rev. B **84**, 155413 (2011).
[33]C. Ataca, M. Topsakal, E. Aktürk, and S. Ciraci, J. Phys. Chem. C **115**, 16354 (2011).
[34]P. Giannozzi, S. de Gironcoli, P. Pavone, and S. Baroni, Phys. Rev. B **43**, 7231 (1991).
[35]X. Gonze and C. Lee, Phys. Rev. B **55**, 10355 (1997).
[36]Y. Wang, J. J. Wang, W. Y. Wang, Z. G. Mei, S. L. Shang, L. Q. Chen, and Z. K. Liu, J. Phys. Condens. Matter **22**, 202201 (2010).
[37]D. Sánchez-Portal and E. Hernández, Phys. Rev. B **66**, 235415 (2002).
[38]The calculation of the electron-phonon interaction has been performed using a 9×9 supercell and a double-zeta polarized (DZP) basis for the electronic Bloch states. For the polar LO phonon, a 17×17 supercell was required to capture the long-wavelength limiting behavior of the electron-phonon coupling due to long-range Coulomb interactions. This calculation must be done with Dirichlet boundary conditions, i.e., $V(\mathbf{r}) = 0$, on the boundaries in the nonperiodic direction perpendicular to the layer in order to avoid interlayer contributions to the potential in the long-wavelength limit.
[39]T. Kawamura and S. Das Sarma, Phys. Rev. B **45**, 3612 (1992).
[40]D. K. Ferry, *Semiconductor Transport* (Taylor and Francis, New York, 2000).
[41]For nondegenerate carriers at room temperature $\langle \varepsilon_{\mathbf{k}} \rangle \sim 26$ meV implying that $k \sim 0.03 \times 2\pi/a$ is a good measure for the wave vector of the carriers. With a maximum phonon frequency of $\sim$50 meV, the phonon wave vectors will be restricted to the interval $0 \leqslant q \leqslant q_{\max}$, where $q_{\max} \simeq 0.1 \times 2\pi/a$ is the phonon wave vector in a backscattering process with $q = 2k$.
[42]O. Madelung, *Introduction to Solid State Physics* (Springer, Berlin, 1996).
[43]J. Sjakste, V. Tyuterev, and N. Vast, Phys. Rev. B **74**, 235216 (2006).
[44]V. Tyuterev, J. Sjakste, and N. Vast, Phys. Rev. B **81**, 245212 (2010).
[45]K. M. Borysenko, J. T. Mullen, E. A. Barry, S. Paul, Y. G. Semenov, J. M. Zavada, M. B. Nardelli, and K. W. Kim, Phys. Rev. B **81**, 121412 (2010).
[46]N. Mori and T. Ando, Phys. Rev. B **40**, 6175 (1989).
[47]H. Rücker, E. Molinari, and P. Lugli, Phys. Rev. B **45**, 6747 (1992).
[48]H. Smith and H. H. Jensen, *Transport Phenomena* (Oxford University Press, Oxford , 1989).
[49]D. L. Rode, in *Semiconductors and Semimetals*, edited by R. K. Willardson and A. C. Beer (Academic Press, New York, 1975), Vol. 10, pp. 1–89.
[50]D. K. Ferry and S. M. Goodnick, *Transport in Nanostructures*, 2nd ed. (Cambridge University Press, Cambridge, 2009).
[51]In order to define a momentum relaxation time $\tau_{\mathbf{k}}$, the collision integral in Eq. (21) must be put on the form $\partial_t f_{\mathbf{k}}|_{\text{coll}} = -\delta f_{\mathbf{k}}/\tau_{\mathbf{k}}$. For inelastic scattering processes, this is, in general, not possible since the in-scattering part of the collision integral depends on the deviation function $\psi_{\mathbf{k}\pm\mathbf{q}} = \psi(\varepsilon_{\mathbf{k}} \pm \hbar\omega_{\mathbf{q}})$.
[52]The sum over $\mathbf{q}$ in Eqs. (22) and (30) have been evaluated using a Lorentzian of width $\Gamma = 3$ meV to represent the δ function: $\delta(\varepsilon_{\mathbf{k}'} - \varepsilon_{\mathbf{k}}) \to 1/\pi \times \frac{1}{2}\Gamma/[(\varepsilon_{\mathbf{k}'} - \varepsilon_{\mathbf{k}})^2 + (\frac{1}{2}\Gamma)^2]$.
[53]D. Jena and A. Konar, Phys. Rev. Lett. **98**, 136805 (2007).
[54]W. G. Aulbur, L. Jönsson, and J. Wilkins, in *Solid State Physics*, edited by F. Seitz, D. Turnbull, and H. Ehrenreich (Academic Press, New York, 2000), Vol. 54, p. 1.
[55]C. Ataca and S. Ciraci, J. Phys. Chem. C **115**, 13303 (2011).
[56]T. Olsen, K. W. Jacobsen, and K. S. Thygesen, e-print arXiv:1107.0600v1 (2011).
[57]G. D. Mahan, *Many-Particle Physics* (Plenum Press, New York, 1990).
[58]F. Giustino, M. L. Cohen, and S. G. Louie, Phys. Rev. B **76**, 165108 (2007).
[59]P. E. Blöchl, Phys. Rev. B **50**, 17953 (1994).